VIENNA UNIVERSITY OF TECHNOLOGY

DEPARTMENT FOR GEODESY
AND GEOINFORMATION

RESEARCH GROUP
REMOTE SENSING

Diplomarbeit

Utilizing the Kp value in the uncertainty estimation of METOP Scatterometer Backscatter Data

Ausgeführt zum Zwecke der Erlangung des akademischen Grades
eines Diplom-Ingenieur/in unter der Leitung von

Univ.Prof. Dipl.Ing. Dr.techn. Wolfgang Wagner
Forschungsbereich Fernerkundung

eingereicht an der Technischen Universität Wien
Fakultät für Mathematik und Geoinformation

von

Albrecht Oppitz

Matrikelnummer 0126672

Glasgraben 1

A-3002 Purkersdorf

Purkersdorf, am 22. Oktober 2015

Abstract

In the TU Wien soil moisture retrieval model the estimated standard deviation (ESD) is a measure for the different error types of the backscatter. This parameter is considered as a noise estimate, incorporating speckle and residual azimuthal effects, based on differences between fore- and after beam of the Advanced SCATterometer (ASCAT) on board the meteorological operational satellite METOP-A. However, for a robust estimate of the estimated standard deviation ESD, time series backscatter data of long period of time is necessary. This can be even up to several years. Thus in this work, the relationship of the current estimation of the standard deviation of the backscatter (ESD) with the standard deviation information (Kp) included in the Metop ASCAT Level 1b backscatter product is analyzed. For a comparison of ESD and Kp a new type of ESD is defined based on the radiometric resolution Kp, denoted as ESD_{Kp}. The elaborate analysis of the two ESD types reveals a nonlinear relation between the ESD and ESD_{Kp}, with much less impact of the azimuthal noise on the ESD_{Kp}. In particular, for arid regions with large azimuthal noise a substantial difference is observed, whereas for rain forests the values of the two ESD quantities are almost equal. As a contrast to the ESD, the value the ESD_{Kp} reaches steady value within a period of few weeks.

Kurzfassung

Im Bodenfeuchte Bestimmungsmodell der TU Wien ist die geschätzte Standardabweichung (ESD) ein Maß für die verschiedenen Fehlerquellen des Radarechos. Unter anderem, werden im Modell das Rauschen der Rückstreuung und Specklemuster berücksichtigt. Weiters werden kleine Einflussgrößen wie die Azimuth Winkelabhängigkeit der Differenz zwischen dem Radarstrahl der vorderen und hinteren Antenne des ASCAT Scatterometers berücksichtigt. Dieses Scatterometer ist Teil der Instrumentenausstattung des meteorologischen Satelliten METOP-A. Für eine stabile Fehlerabschätzung werden Messdaten über lange Perioden, bis zu mehreren Jahren, benötigt.

Daher wird in der vorliegenden Diplomarbeit der Zusammenhang und Unterschied der üblicherweise verwendeten geschätzten Standardabweichung der Rückstreuung (ESD) mit der radiometrischen Auflösung Kp aus dem Metop ASCAT 1b Produkt erarbeitet. Für einen Vergleich der ESD und Kp wird ein neuer ESD Wert auf der Grundlage der radiometrische Auflösung Kp definiert ist, bezeichnet als ESD_{Kp}. Eine genaue Analyse der beiden ESD Werte zeigt eine nichtlineare Beziehung zwischen ESD und ESD_{Kp}, mit einer viel geringeren Auswirkung des azimuthalen Fehlers auf den ESD_{Kp}. Insbesondere wird für trockene Regionen mit großem azimuthalem Fehler ein großer Unterschied festgestellt, während für Regenwälder die Werte der beiden ESD Werte sind fast gleich. Im Unterschied zum ESD, erreicht der ESD_{Kp} Wert ein konstantes Niveau innerhalb weniger Wochen.

Acknowledgments

The present research was accomplished at the Department of Geodesy and Geoinformation, Research Group Remote Sensing, Vienna University of Technology. First of all, I would like to thank all those who contributed to this study.

Special thanks goes to my supervisor Prof. Dr. Wolfgang Wagner for the continuous support of my research, for his patience, motivation, enthusiasm, and immense knowledge. Besides my advisor, I would like to thank the rest of my thesis committee: Dipl.-Ing. Sebastian Hahn und Dipl.-Ing. Christoph Reimer, for their encouragement, insightful comments, and hard questions. Furthermore, I want to thank my brother Berthold Oppitz, he helps me to focus my efforts in the right direction. Finally, I would like to thank my wife Mag. Daniela Oppitz who cordially supported me throughout the study and found the right words for motivation.

Contents

List of Figures

List of Tables

List of Acronyms

ASCAT	Advanced Scatterometer on board METOP-A
ERS	European Remote Sensing Satellite (ESA)
ESA	European Space Agency
ESD	Estimated Standard Deviation
EUMETSAT	European Organisation for the Exploitation of Meteorological Satellites
METOP	Meteorological Operational Satellite (EUMETSAT)
RCS	Radar Cross-Section
SAR	Synthetic Aperture Radar

Chapter 1

Introduction

1.1 Motivation

Water plays a crucial role for all organisms on earth. It acts as solvent in biological cells. Without water metabolism and protein synthesis in cells would be impossible. Also on macroscopic scale water plays an important role, it shapes the topology of the Earth's surface, allows effective transportation needed for many technological processes and enables agriculture. The water on earth exists in different physical states, and is present in different forms in for instance air, oceans, glaciers and ice shields. Water is infiltrated at the soil on earth surface and this resulted soil moisture is crucial for the life on earth. At the areas with very low soil moisture, only very few species are able to survive in such these areas. These organisms are highly adapted to such harsh conditions. Other extreme to these are the rain forests, where the quantity of species is order of magnitude larger.

Global warming leads to a further extend of deserts and steppes, thus the investigation of moisture on earth's surface is of mayor importance. The on site based measurements are only available for limited locations on the

Earth's surface. Therefore, the need for a method with global disposability of soil moisture data is substantial. Preferably such a method should have the ability to estimate the temporal variability of the soil moisture. Now for several years, this requirement is achieved by spaceborne scatterometer, observing the Earth's surface. Such scatterometer send an electromagnetic pulse towards the Earth and measures the echo scattered from the Earth's surface. Sophisticated models are then applied on the data measured with the scatterometer signal in order to derive soil moisture. Using spaceborne scatterometer for soil moisture estimation has the advantage of accessing the whole Earth's surface.

The backscatter data provided by the ASCAT scatterometer depends on different factors, such as measurement geometry, vegetation canopy, surface roughness and soil moisture. The impact of these factors on the backscatter measurement is of different magnitude and time scales. This noise level of the backscatter contains information on the Earth's surface. However, this estimation is a static value, which does not reflect temporal effects. In this work the so far unused Kp value is incorporated in the computation of the overall backscatter variance. This master thesis represents a first proof of concept study utilizing the Kp value in the uncertainty estimation.

1.2 Objective and structure of thesis

In the TU Wien soil moisture retrieval model the estimated standard deviation (ESD) is an estimate of the uncertainty of the measuresed backscatter value. This parameter considered noise, speckle and the residual azimuthal effects, based on difference between for- and aft-beam of the Advanced SCAT-terometer (ASCAT). The idea and research question of this master thesis was to investigate the relationship and differences of the current estimated standard deviation (ESD) of backscatter in the TU Wien soil moisture retrieval with the standard deviation information (Kp value) included in the Metop ASCAT Level 1b backscatter product. Maybe in the future the uncertainty estimation of backscatter can be enhanced by incorporating the Kp value in the computation of the overall backscatter variance. This master thesis shows a way how the Kp value can be utilized in the uncertainty estimation.

The work is structured as follows: In chapter 1 a brief induction about the ASCAT soil moisture products is given. In chapter 2 the working principles of the MetOp ASCAT instrument and its measurement geometry are explained in addition to the definition of the ASCAT products. Furthermore, a detailed description on the radiometric resolution Kp is given followed by a summary on the noise model used by the TU Wien soil moisture retrieval method. Finally, a new type of the estimated standard deviation of the backscatter is introduced, based on the Kp-value. Moreover, characterisitcs of the study areas are presented in detail. In chapter 3 detailed analysis of the backscatter and radiometric resolution data are presented. This is followed by the concluding remarks in chapter 4.

Chapter 2

Methology

2.1 MetOp ASCAT

2.1.1 Introduction

MetOp is a series of three polar orbiting meteorological satellites, representing the space segment component of the EUMETSAT Polar System (EPS). MetOp-A (launched on 19 October 2006) and Metop-B (launched on 17 September 2012) are in a lower polar orbit. They are located at an altitude of 817 km to provide more detailed observations of the global atmosphere, oceans and continents. MetOp-C is due to be launched in 2017 [1]. The Advanced Wind Scatterometer (ASCAT) is a radar instrument with six fan-beams and it is carried on board the EUMETSAT MetOp (meteorological operational) series of satellites. It is designed to accurately measure the surface backscatter allowing the retrieval of wind fields over the ocean [2]. The data provided by ASCAT is also used by a number of other applications including sea ice monitoring and soil moisture retrieval [3], [4].
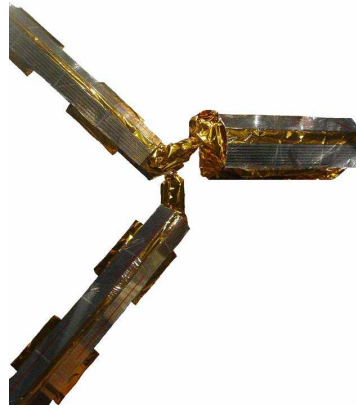
Figure 2.1: The three antenna assemblies of the ASCAT Instrument.

The following section describes the ASCAT system and gives an overview of the instrument, the geometry, the ASCAT data products and the resolution of the scatterometer measurements.

2.1.2   Instrument description

The ASCAT instrument has been primarily designed to operationally provide ocean wind vectors. Wind scatterometer already flown on ESA's ERS-1 and ERS-2 satellites have demonstrated the worth of such instruments for global determination of sea-surface wind vectors. The successor of the ERS-1/2 scatterometer, the Advanced SCATterometer (ASCAT) is the result of developments of more than twenty years. The ASCAT instrument is a real aperture radar, operating at 5.255 GHz (C-band) and using six vertically polarized antennas. There are two antenna assemblies each containing three antennas. The ASCAT instrument operates in two different modes: Measurement and Calibration mode. The nominal instrument mode, and the
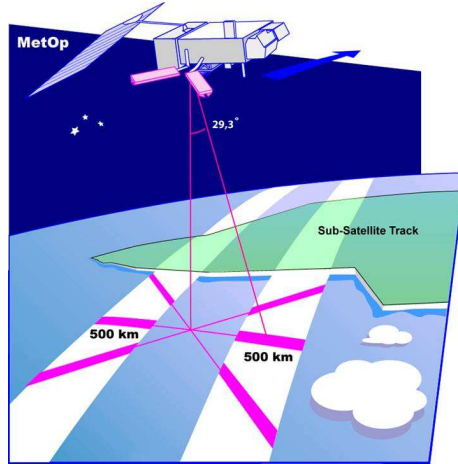
Figure 2.2: Viewing geometry of the ASCAT instrument onboard METOP [5].

only one that generates science data for the users, is measurement mode. In this mode all six antennas are activated in sequence. The echo, internal calibration and noise samples are recorded from each of them. In contrast to the scatterometer used on ERS, ASCAT transmits a long pulse with Linear Frequency Modulation. After de-chirping the received echo from the ground, the backscattered signal is spectrally analyzed and detected. These methods rely on a Fourier transformed signal which is used to produce a power spectrum as a function of range. This is then averaged along track and transmitted to the ground along with ancillary data.

The instrument was developed under ESA/EUMETSAT contract by EADS Astrium in Friedrichshafen, Germany.

2.1.3   Geometry

Measurement geometry is a very important factor in the further data processing. The ASCAT system geometry is based on the robust and well-
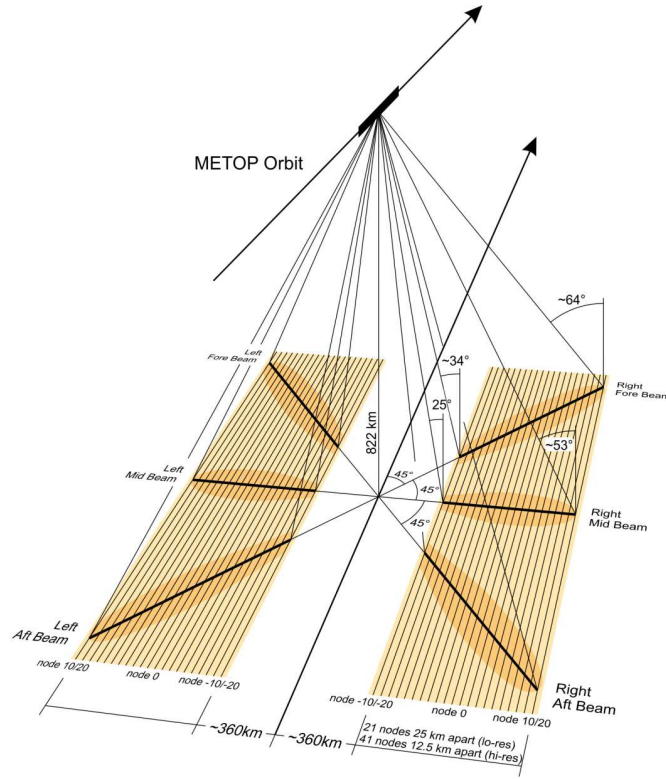
Figure 2.3: Measurement geometry of METOP-A ASCAT [5].

understood concept of the ERS scatterometer. It covers two 500 km swaths which are separated from the satellite ground track by about 336 km for the minimum orbit height of 822 km (see Figure 2.3). The ASCAT incidence angle ranges from 25° to 65° (see Figure 2.3). For each swath, three antennas illuminate the surface at three different azimuth angles, measuring the backscattered signal. At such incidence angles, the main backscattering mechanism over the ocean is considered to be Bragg resonance, which describes the interaction of the radar signal with short sea surface waves having a wavelength of few centimeters [6].
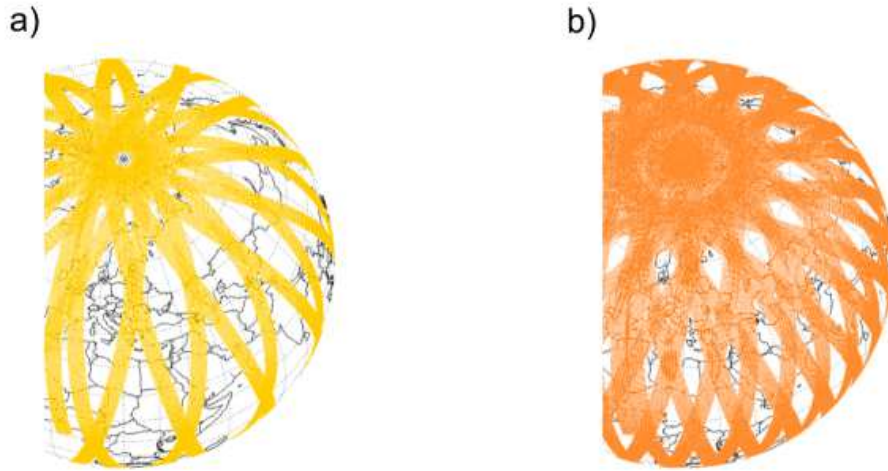
Figure 2.4: Daily cover ERS-1/2 (a) and METOP-A (b) [7].

2.1.4   ASCAT data products

Compared to the predecessors on ERS-1 and ERS-2 the advanced measurement geometry of ASCAT allows twice the cover and, thus the daily cover increases from 41% to 82% (see Figure 2.4). The spatial resolution was improved from 50 km to 25 km, with the same radiometric accuracy as the ERS-1/2 scatterometer. Three backscatter measurement, corresponding to the for, mid and aft antenna, are obtained from each point on the Earth's surface inside one of the two swaths within a short time delay [8] , called in the following as, triplet. The radar echo signal of the scatterometer is transmitted to the ground station , where it is transformed into backscatter coefficients.

Some of the key parameters driving the instrument design are related to the desired radiometric characteristics of the normalized backscatter determination [9]: (1) radiometric resolution (Kp) describes the uncertainty in

a σ^0 estimate due to speckle and thermal noise; (2) radiometric accuracy describes the maximum uncertainty in the σ^0 estimates, once the statistical noise has been averaged out.

Global data products are classified in different levels according their processing progress. ASCAT provides the following product levels [10].

- **Level 0:** Unprocessed raw instrument data from the spacecraft. These are transmitted to the ground stations in binary form.

- **Level 1a:** Reformatted raw data together with already computed supplementary information (radiometric and geometric calibration) for the subsequent processing.

- **Level 1b:** Calibrated, georeferenced and quality controlled backscatter coefficients σ^0 in full resolution or spatially averaged. It includes also ancillary engineering and auxiliary data.

- **Level 2:** Georeferenced measurements converted to geophysical parameters, at the same spatial and temporal resolution as the Level 1b data.

- **Level 3:** Geophysical products derived from Level 2 data, which are either resampled or gridded points.

The first product of the intermediate level 1 in the ASCAT data process chain is the so called full resolution product. The main geophysical parameter of the level 1b is the normalized backscatter coefficient σ^0. Each antenna projects 256 σ^0 values on the Earth'ssurface. The Doppler pattern over the
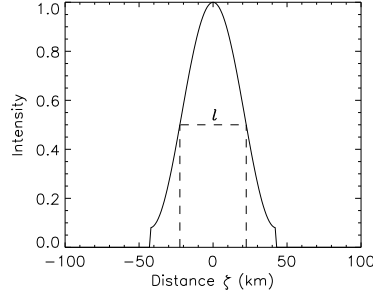
Figure 2.5: Hamming window function used for spatial filtering. Dashed lines marks the spatial resolution [13].

surface result in a footprint size of about 10×20 km with various shapes and orientations. The radiometric accuracy and the inter-beam radiometric stability is expected to be less then 0.5 dB peak-to-peak [11].

In addition, the level 1b product offers averaged backscatter coefficients σ^0 at two different spatial grids. For spatial filtering a two dimensional Hamming window function H(x,y) = H(x)H(y), centered at every grid node, is used. The window function in one dimension is given by

$$H(x) = 0.54 + 0.46 \cos(\frac{\pi x}{L}) \tag{2.1}$$

where x is the distance to the center of the window and L is the radius of the window. The full resolution data is averaged over a square with a side length of approximately 85 km [12]. The spatial resolution is defined as the distance where the Hamming window function reaches 50% of its maximum intensity (see Figure 2.1).

After the generation of the swath nodes and the spatial averaging two products are offered by the ASCAT level 1b. The so called nominal product with a grid spacing of 25 km and 21 nodes in each line per swath, resulting
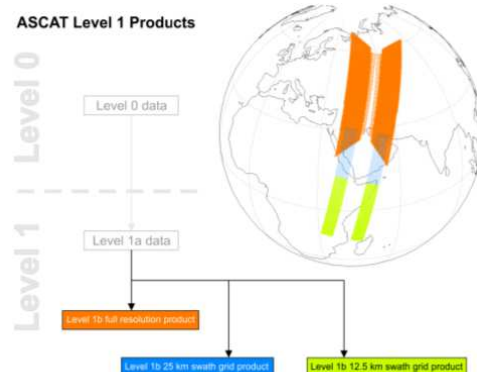
Figure 2.6: Overview of ASCAT level 1 products [5].

in a spatial resolution of 50 km for each grid point. In addition, a research product is provided with a spatial resolution ranging from 25 to 36 km and a grid spacing of 12.5 km resulting in 41 nodes per swath line.

The ASCAT level 2 ground processing products are generated from backscatter values by applying geophysical models. Over ocean surfaces the near-surface wind vectors are retrieved by relating the wind speed and direction to the σ^0 values. The inverse algorithms used for the computation of the wind vectors yield in ambiguities of the solutions, which is difficult to solve exactly. On land surfaces the σ^0 values can be used to derive to soil moisture data based on a geophysical model developed by the Department of Geodesy and Geoinformation of the Vienna University of Technology.

2.2 TU Wien Soil moisture retrieval method

The backscatter signal measured by ASCAT over land is influenced by various factors like surface roughness, vegetation structure, vegetation water content,

and soil moisture on different time scales. The surface roughness is considered as time-invariant. The time-scale of surface soil moisture variation is hours or days, whereas the vegetation structure and the vegetation water content changes within several days or weeks.

Various models have been proposed to calculate σ^0 from vegetated surface based on Radiative transfer theory [14] [15] [16]. Radiative transfer theory describes the interaction of electromagnetic waves with matter, propagating through a medium. In general, absorption, emission and scattering processes have to be considered. A problem of these complex theoretical models is that many parameters are required [17] in order to solve the basic equations.

In 1998 Wagner *et al.* [13] presented the TU-Wien soil moisture retrieval method which is basically an empirical model based on change detection. The model parameters of the TU-Wien soil moisture retrieval method are determined from long backscatter time series, which greatly simplifies the problem compared to the physical inversion models.

The backscatter σ^0 depends on the look geometry of the ASCAT antenna described by the azimuth and incidence angle, which varies from acquisition to acquisition. This intensity of the backscatter signal increases strongly with decreasing incidence angle. To compare the backscatter coefficients directly they have to be normalized to a reference incidence angle. However, the incidence angle dependency of backscatter is not proportional to soil moisture. The vegetation density has an impact on the shape of the incidence angle dependency of backscatter depending on the type and density of vegetation as well as the orientation of vegetation elements, as illustrated in Figure 2.7.

A second order polynomial is sufficient to describe the backscatter - incidence angle behavior of such a curve. A Taylor polynom with an expansion
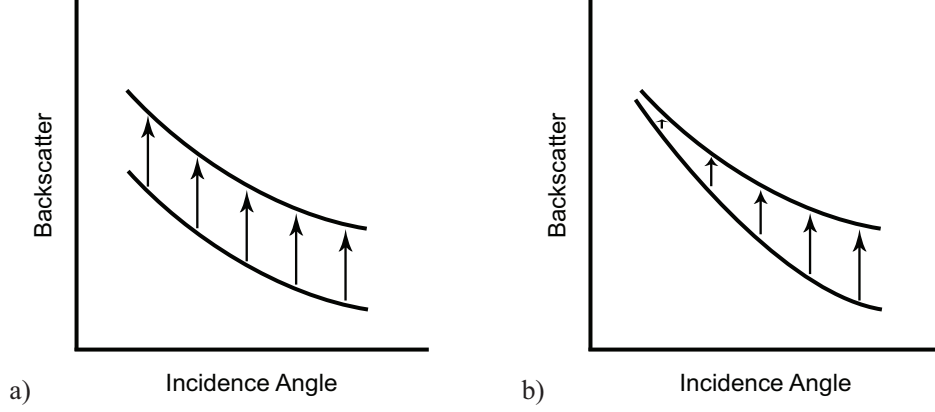
Figure 2.7: Incidence angle dependency of backscatter a) soil moisture change b) vegetation change.

point at 40° leads to:

$$\sigma^0(\theta, t) = \sigma^0(40, t) + \sigma'(40, t)(\theta - 40) + \frac{1}{2}\sigma''(40, t)(\theta - 40)^2 \qquad (2.2)$$

where σ' and σ'' denotes the first and second derivative of $\sigma^0(\theta, t)$ with respect to θ. The σ' and σ'' are sensitive to the vegetation and surface structure, whereas it is assumed to be independent of the dielectric properties [18]. The multi-incidence angle capability of ASCAT is used to determine the slope σ' and curvature σ'' from the local slope values extracted from simultaneous observations. The local slope can be derived individually by linear fitting, using the σ^0 triplet:

$$\sigma_L^0(\theta_L) = \frac{\sigma_m^0(\theta_m) - \sigma_{f,a}^0(\theta_{f,a})}{\theta_m - \theta_{f,a}}, \qquad (2.3)$$

where

$$\theta_L = \frac{\theta_m + \theta_{f,a}}{2}$$

The indices f , m and a denote the *for-* *mid-* and *aft*-beam of the instrument. To determine the temporal behavior of slope σ' and curvature σ'', the local slope values σ_L are calculated for each individual σ^0 triplet using neighboring

measurements in a given period τ centered on a selected day t. A linear fit through all local slope values σ_L^0 in this time window τ reveal the slope $\sigma^0(40, t)$ and curvature $\sigma^0(40, t)$ parameter at a 40°incidence angle.

The effect of changes in soil moisture and vegetation on the backscatter-incidence angle dependence $\sigma^0(\theta)$ is illustrated in Figure 2.7. It is assumed that, soil moisture changes do not alter the backscatter shape. More dense vegetation increases the backscatter intensity for far and mid incidence angles, whereas for near incidence angles the intensity decreases due to the attenuation of volume scattering from the vegetation canopy. This behavior is illustrated in Figure 2.8. At the two characteristic angles $\theta_{dry} = 25,$° and $\theta_{wet} = 40$° the two curves corresponding to dormant and fully developed vegetation show a crossover for dry and wet soil, respectively. This allows to compensate the vegetations effects, as at these two angles vegetation growth has more or less no influence on the backscatter coefficient.

The result of the TU Wien soil moisture retrieval method is relative soil moisture, which is scaled between the lowest σ_{dry}^0 and highest σ_{wet}^0 of the available backscatter time series.

For a robust estimation of the dry and wet reference, an accurate removal of outliers is important. In the improved algorithm the number of observations, which are used for the determination of the dry and wet-reference, is selected with respect to an explicit uncertainty range, defined as a 95% 2-sided confidence interval of the measurements. This is done by separating the extreme low values in σ_{dry}^0 and the extreme high values in σ_{wet}^0. The confidence interval of the extreme low and high values are obtained by considering the noise of σ_{dry}^0 and σ_{wet}^0:

$$\text{Confidence Interval} = \pm 1.96 \times (\text{Noise of } \sigma^0(\theta)) \qquad (2.4)$$

The value in the Equation 2.4 represents the 97.5 percentile of the standard
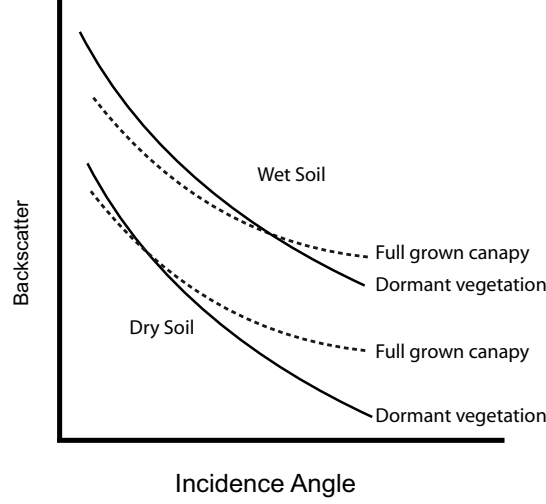
Figure 2.8: Crossover.

normal distribution. The dry and wet references at the crossover angles are given by the mean values of the separated extreme values:

$$\sigma^0_{dry} = \frac{1}{N_{lower}} \sum_{j=1}^{N_{lower}} \sigma^0_j(\theta_{dry}), \tag{2.5}$$

$$\sigma^0_{wet} = \frac{1}{N_{upper}} \sum_{j=1}^{N_{upper}} \sigma^0_j(\theta_{wet}), \tag{2.6}$$

where N_{lower} and N_{upper} are the number of low and high extreme values separated according the confidence interval. Only the dry reference σ^0_{dry} has to be transformed back to the normalization angle according Equation 2.2. By scaling the values $\sigma^0(40,t)$ between $\sigma^0_{wet}(40,t)$ and $\sigma^0_{dry}(40,t)$ the relative surface soil moisture is given by:

$$m_s(t) = \frac{\sigma^0_{wet}(40,t) - \sigma^0_{dry}(40,t)}{\sigma^0_{wet}(40,t) - \sigma^0_{dry}(40,t)}. \tag{2.7}$$
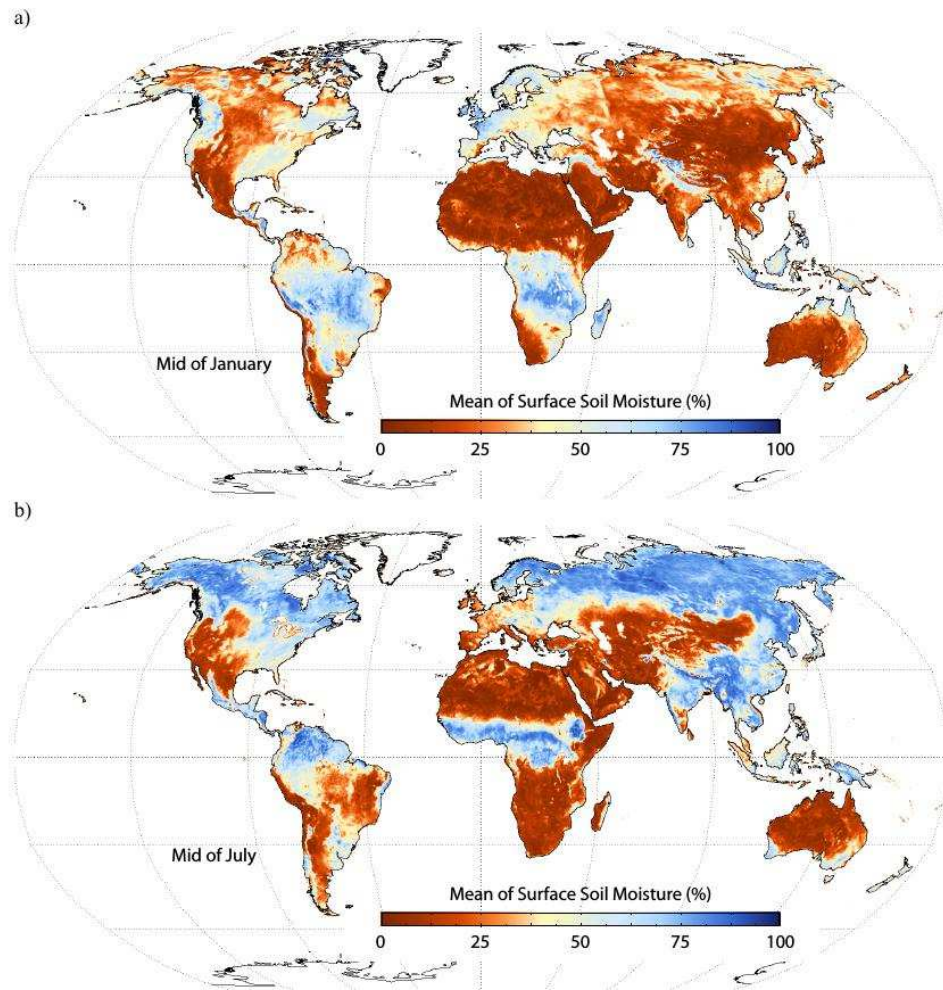
Figure 2.9: The estimated soil moisture in mid of; a) January and b) July averaged over the long-term scatterometer observations from August 1991 to May 2007 [18].

Figure 2.9 shows the estimated soil moisture for (a) mid of January and (b) July averaged over the long-term scatterometer observations from August 1991 to May 2007.

2.3   Kp - the radiometric resolution

2.3.1   Definition of Kp

The performance of scatterometer systems, i.e., their radiometric resolution, is given by the Kp parameter [19]. The Kp value of the instrument describes the ability of the sensor to differentiate the variability of the backscattered power. It is defined as the normalized standard deviation associated to the σ^0 measurement in the linear domain. Thus, the unit of the radiometric resolution Kp is [%]. In particular, the Kp value is calculated for all three beams $b \in (for, mid, aft)$ of the ASCAT instrument by

$$Kp_{i,b} = \frac{\sqrt{Var[\sigma_{i,b}^0]}}{\overline{\sigma}_{i,b}^0} \tag{2.8}$$

where $\sigma_{i,b}^0$ is the backscattering coefficient, its mean is denoted as $\overline{\sigma}_{i,b}{}^0 = mean\left(\sigma_{i,b}{}^0\right)$ and the i labels the individual measurement in a resampling window. The integration area of $\overline{\sigma}_{i,b}{}^0$ is defined by the two dimensional window function $H(x,y)$, were $H(x)$ is given by Equation 2.1. The Kp value is an engineering parameter reflecting the instrument efficiency.

2.3.2   Noise characterization of backscatter measurements

When performing backscatter measurements, the scatterometer transmits a microwave pulse and the backscattered signal power $\widehat{P_R}$, which is reflected

from the surface is measured. In addition, a noise-only power measurement $\widehat{P_N}$ is performed, as $\widehat{P_R}$ is affected by instrument noise as well as noise induced by geophysical phenomena due to the surface anisotropy, as well as other error types, for instance errors caused by speckle [20]. Subtracting the noise-only measurements form the measured signal results in the backscattered signal power $\widehat{P_S}$ i.e., $\widehat{P_S} = \widehat{P_R} - \widehat{P_N}$. The backscattering coefficient σ^0 are calculated from the signal power $\widehat{P_S}$, using the radar equation

$$\sigma^0 = X\widehat{P_S} \tag{2.9}$$

where

$$X = \frac{(4\pi)^3 R^4 G_p}{P_T \lambda^2 L_s G^2 A_c} \tag{2.10}$$

where R is the range from the scatterometer to the observation cell, G_p is the system gain, P_T is the transmitter power, λ is the radar wavelength, L_S, is the system loss, G is the antenna gain, and A_c, is the resolution element (cell) area. In general, σ^0 is a function of the incidence angle of the measurements, with larger incidence angles generally producing smaller σ^0 values.

Noise only measurements are performed routinly by ASCAT in an internal loop.

Any error in the backscattered signal power and the noise-only power measurement, as well as in the radar equation parameters, result in an error in σ^0. The total variability of σ^0 may be described by the Kp parameter which is defined as the normalized standard deviation of the measurement [21].

2.3.3   Speckle

One source of error in the radar backscatter signal is called speckle. The phenomenon speckle is caused by interference effects of coherent radar systems due to surface roughness on the scale of the transmitted electromagentic waves. For the hypothetical case of of an radar illuminating only two reflecting points separated by a small distance d, the received field strength E at the radar with a much larger distance to the points as their separation is given by [22].

$$|E| = 2\left| E_0 \cos\left(\frac{2\pi d}{\lambda}\sin\theta\right)\right| \tag{2.11}$$

where λ denotes the wavelength of the electromagentic wave and θ is the angle of radar beam with respect to the surface normal.

As the wave interacts with a target, each scatterer contributes a backscattered wave with a phase and amplitude change. The total returned modulation of the incident wave is the summation over the number of scatterers illuminated by the beam. Hence, the observed signal will be affected by interference effects as a consequence of the phase differences between the scatterers. In fact, speckle can be understood as an interference phenomenon in which the principal source of the noiselike quality of the observed data is the distribution of the phase terms [22].

2.4   Error characterization of the TU Wien soil moisture model

2.4.1   Introduction

The TU Wien soil moisture retrieval method in section 2.2 includes an error model to quantify uncertainties related to measurements in the retrieval algorithm. Naeimi [18] categorizes the error sources in the TU-Wien soil moisture retrieval algorithm as:

- uncertainties linked to the data acquisition including backscatter noise, uncertainty of the gain parameters, geometry, and data resampling;

- uncertainties associated with the geophysical model function.

These error sources are propagated through the retrieval algorithm by simple error propagation. Therefore, the estimated standard deviation is exploit as an uncertainty estimate of the backscatter to initialise the error propagation of the soil moisture retrieval algorithm. This allows the determination of the noise of the soil moisture.

2.4.2   Azimuthal anisotropy

The intensity of the backscattered signal from an rough surface depends on the azimuthal look angle. Two of the three antennas of ASCAT have the same incident angle but differ in the azimuthal look angle (*for-* and *aft*-antennae). The difference in the *for-* and *aft*-backscattering coefficient

depends on the different azimuthal angle and the noise level of the individual σ^0 measurements [23] , given by

$$\delta = \sigma^0_{aft} - \sigma^0_{for} \tag{2.12}$$

where $\sigma^0{}_{for}$ and $\sigma^0{}_{aft}$ denote the *for*- and *aft*-beam backscatter. If a large number of backscattering pairs (for and aft beam) are available, then the average of δ is an indication of surface anisotropy. The backscatter $\sigma^0{}_{for}$ and σ^0_{aft} are supposed to be normally distributed variables [24], therefore their difference δ is also normally distributed [25] (see Figure 2.12).

2.4.3 Estimated Standard Deviation of the Backscattering Coefficient

All three beams of ASCAT observe the same target, and the *for*- and the *aft*-beam share the same incidence angles. Thus, as long as there are no azimuthal effects, the backscatter measurement $\sigma^0_{for/aft}$ of the *for*- and *aft*-beam, respectively, are comparable, i.e., statistically speaking, they are instances of the same distribution. We assume that σ^0_{for} and σ^0_{aft} are normally distributed in the logarithmic range [24]. Since both *for*- and *aft*-antenna have the same incidence angle, the expectation of the random difference is

$$\delta := E\left(\sigma^0{}_{for} - \sigma^0{}_{aft}\right) = E\left(\sigma^0{}_{aft} - \sigma^0{}_{for}\right) = 0 \tag{2.13}$$

and its variance is twice the variance of one of the beams [25]. This can be
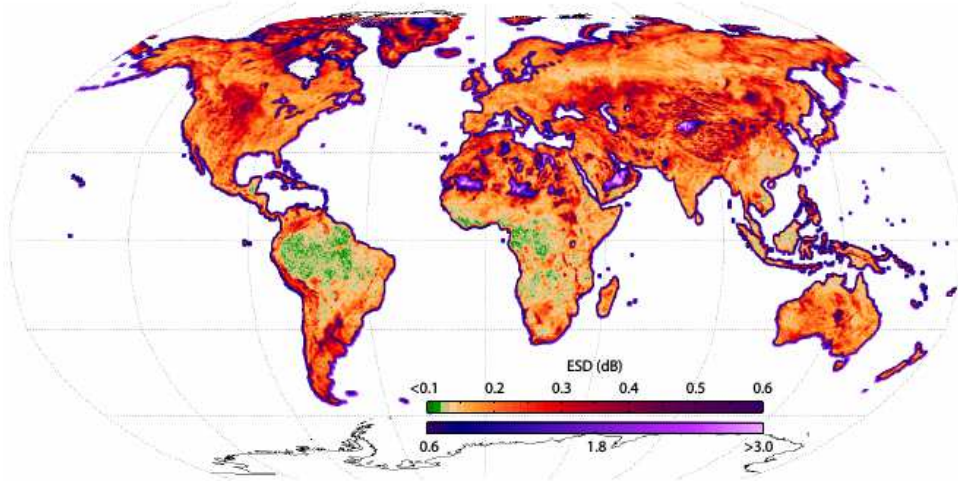
Figure 2.10: Global distribution of ESD [26].

derived using an inverse error propagation [27] on $\delta(\sigma_{for}^0, \sigma_{aft}^0)$ as given by [28]

$$Var\left(\delta\right) \approx Var\left(\sigma^0{}_{for}\right) + Var\left(\sigma^0{}_{aft}\right) = 2 \cdot Var\left(\sigma^0\right) \tag{2.14}$$

Rewriting Equation 2.14 gives the following expression for the variance of σ^0

$$Var\left(\sigma^0\right) = \frac{Var\left(\delta\right)}{2}. \tag{2.15}$$

Furthermore, the estimated standard deviation can be given as follows:

$$ESD\left(\sigma^0\right) = \sqrt{\frac{Var\left(\delta\right)}{2}} \tag{2.16}$$

The ESD represents an estimate of the real standard deviation of the backscatter intensity.
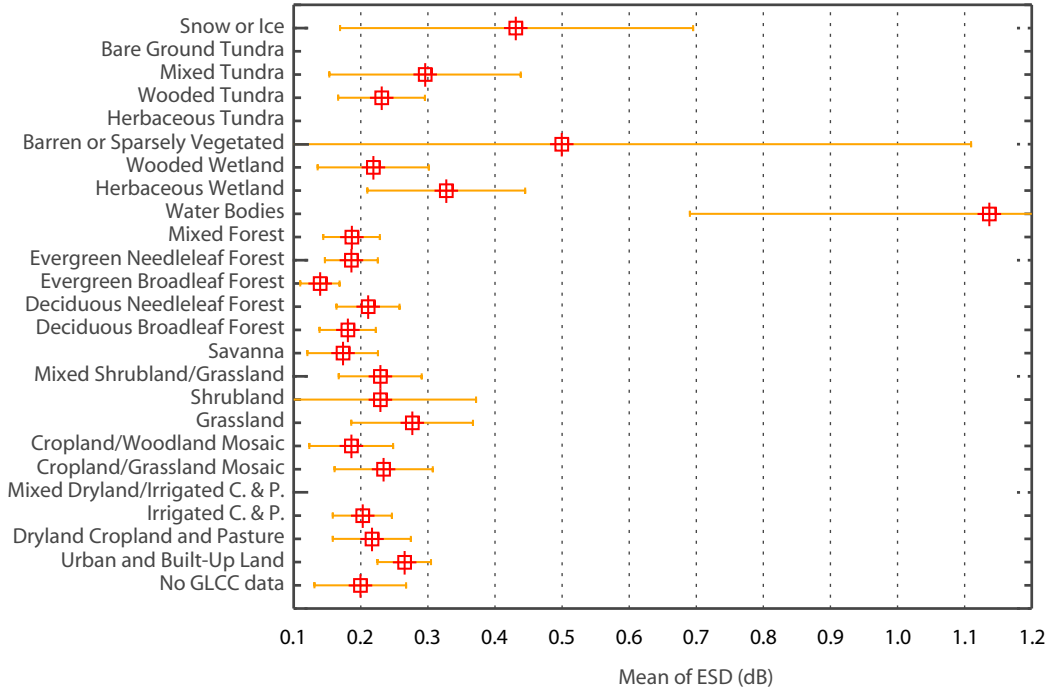
Figure 2.11: ESD values averaged for different land cover classes [18].

The global distribution of the ESD calculated by Naeimi [29] is exemplified in Figure 2.10 and Figure 2.11 shows the ESD values determined for various land cover classes [30].

2.4.4   Azimuthal error sources

In the TU-Wien model any kind of residual azimuthal discrepancy in backscatter is considered as noise. Naeimi [18] identifies different types of error sources influencing the azimuthal noise.

Instrumental noise

The instrumental noise of ASCAT is determined by measuring backscatter coefficients over rainforest's, as they behave like a volume scatterer over a

wide range of incidence angles. The instrument noise has random behavior with a Gaussian distribution, and is approximated by an value of about 0.13 dB.

Influence of Land Cover on the Azimuthal Noise

The topography of the Earth's surface and the three dimensional architecture of vegetation have a clear influence on the azimuthal noise. Naeimi [18] used three global datasets (a) Global Land Cover Classification Data, (GLCC) [31], (b) Global Lakes and Wetlands Database, (GLWD) [32] and (c) Global Digital Elevation Data, (GTOPO30) [33] to determine the influence of the surface characteristics on the azimuthal noise. The influence of the land cover classes on the ESD is shown in Figure 2.11.

Water

Backscatter from water depends on its surface roughness. The main contribution to the backscatter difference of the for- and aft-antennae do not come from large waves, but rather from little water ripples on the surface [34]. Naeimi demonstrated an increase of the mean ESD with increasing coverage of water bodies for inland water, open water, herbaceous wetland, floodplain and marsh.

Desert-Sand Dunes

The same anisotropy like the one found over the open water is also observable over sand desert areas. But in contrast, the backscatter is more complex, as microwaves penetrates deeper into soil, which is inverse proportional to the wetness condition. Thus with increasing moisture amount during the raining season the backscatter regularly increases. Like on water surfaces, the azimuthal response is sensitive to the orientation of small sand ripples. Naeimi observed a pronounced increase of the mean ESD with increasing sand desert coverage.

Urban and Built-Up Land

Backscatter intensity from urban areas are higher as their surroundings, as rectangular aligned surfaces reflects the energy back in the direction of the emitter. Due to multiple reflections an increase of azimuthal noise is also observed.

Dense Vegetation

In contrast the azimuthal noise of dense vegetation decreases with increasing coverage. Furthermore, the quantity of biomass as well as three dimensional architecture of the vegetation have an impact on the azimuthal noise. The minimum value of ESD is observed in ares covered by dense vegetation, where the volume scattering is dominant.

Topography

A further azimuthal error source is the topography of the Earth's surface. The backscatter intensity reaches a maximum for surfaces normal to the look direction of the scatterometer antennas and decreases for more oblique look direction in relation to the surface orientation. This leads to an increase of the azimuthal noise in areas with complex topography. 2

Snow Cover and Frozen Soil

The freezing of soil results in a strong decrease of the backscatter intensity. When the surface is covered with snow the situation becomes more complex. Dry snow is more or less transparent at C-Band, subsequently the reflections are affected by the soil under the snow cover. For wet snow the dominant mechanism is surface scattering and the azimuthal noise depends on the roughness of the snow surface.

2.5   Variance and mean of a mixture of normal distributions

In Equation 2.12 we are considering the difference of two normally distributed random variables. Thus a framework to estimate the distribution function of normal distributed random variables and their mixtures is necessary. Following Java Behboodian [35], a connection between variance and mean of a mixture of normal distributions is described in this section.

In a mixture of k normal distributions the maximum likelihood estimates of μ_i and σ_i^2, and for $i = 1, \ldots, k$, can be expressed by a weighted (p_i) sample mean and a weighted sample variance, and the maximum likelihood estimates of the over-all mean and variance of the mixture coincide with the sample mean and sample variance. The probability density function of a mixture of k normal distributions is

$$f\left(x\right) = \sum_{i=1}^{k} p_i \cdot f_i\left(x\right) \qquad (2.17)$$

where, for $i = 1, \ldots, k$

$$f_i\left(x\right) = \frac{1}{\sqrt{2\pi}\sigma_i} \cdot e^{\frac{-(x-\mu_i)^2}{2\sigma_i^2}}$$

$$0 < p_i < 1, \quad \sum_{i=1}^{k} p_i = 1$$

The overall mean μ and variance σ^2 of the mixture, say α and β, are

$$\alpha = \sum_{i=1}^{k} p_i \cdot \mu_i \qquad (2.18)$$

$$\beta = \sum_{i=1}^{k} p_i \cdot \left(\sigma_i^2 + \mu_i^2 \right) - \left(\sum_{i=1}^{k} p_i \cdot \mu_i \right)^2 \tag{2.19}$$

Let $x_1, \ldots, x_n$ be the experimental values of a random sample from a distribution with density $f(x)$ and let

$$\overline{x} = \sum_{i=1}^{n} \frac{x_i}{n} \tag{2.20}$$

$$s^2 = \sum_{i=1}^{n} \frac{(x_i - \overline{x})^2}{n} \tag{2.21}$$

be the sample mean and sample variance.

Behboodian [35] gives a proof for the two results:

1. The maximum likelihood of estimates of μ_i and σ_i^2 can be expressed by a weighted sample mean and a weighted sample variance.

2. The maximum likelihood estimates of α and β are $\overline{x}$ and s^2.

Figures 2.12 exemplifies the maximum likelihood estimate of α and β, applied to the difference of the experimental values X_i of a normally distributed random sample. In the bottom panel (b) the normally distributed random variables are shown as histograms (X_i^1 and X_i^2), as well as the difference of the experimental values $X_i^1 - X_i^2$. The difference of the normally distributed random variables $X_i^1 - X_i^2$ is normally distributed [25]. The probability function of the normal distributions $f_i(X)$ corresponding to the random samples in (b) and probability function $f(X)$ of the maximum likelihood estimate of
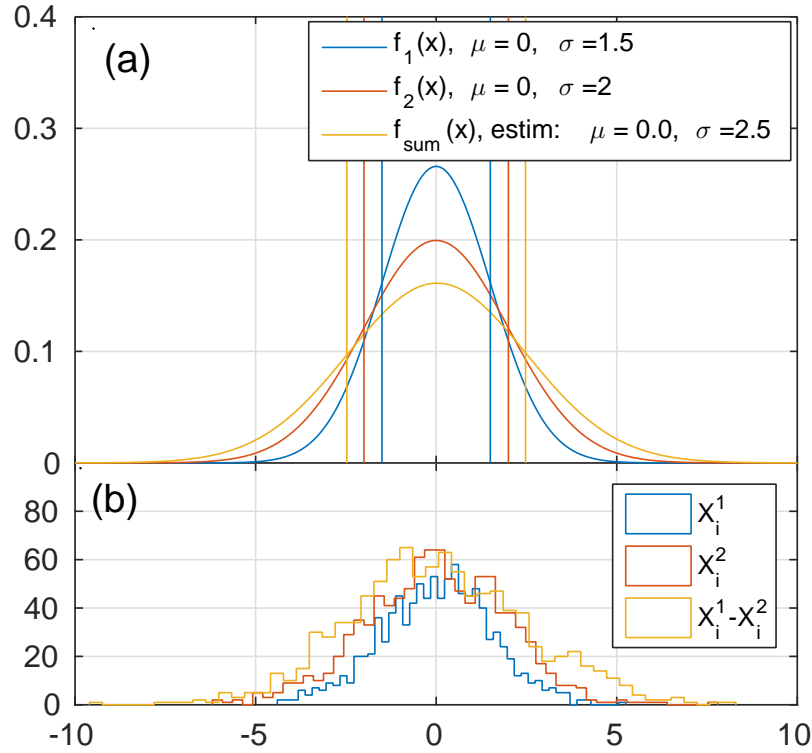
Figure 2.12: (a) Two normal distributions (f1 und f2) with equal mean and different variance and their overall distribution f3. (b): Histogram of three random samples drawn from standard distributions in (a).

the differences of the experimental values are shown in panel (a) by solid lines. The vertical lines indicates the standard deviation of the corresponding probability function. This exemplifies that the difference of two normally distributed random variables is normally distributed (see Equation 2.12).

Figure 2.12 (b) shows three normal distributed random samples X_i as histogram. In the top panel (a) the normal distribution probability density function corresponding to the maximum likelihood of estimates of μ_i and σ_i^2 , indicated by vertical lines, are plotted as dashed lines, whereas the probability density function of the normal distribution $f_i(X)$ in Equation 2.5

are plotted as solid lines.

2.6   The relationship between ESD and Kp

The *ESD* given by Equation 2.16 represents an estimate of the real standard deviation of the backscatter coefficient. It is a temporal invariant value, as it is calculated from long-term time series measurements. If there is an incidence angle bias the ESD would be underestimated, furthermore the calculation of the ESD in Equation 2.16 neglects the backscatter data provided by the mid antenna.

To enhance the uncertainty estimation of the backscatter the Kp value is foreseen to be incorporated in the computation in the overall backscatter variance. Thus it is useful to define an additional ESD_{Kp}, using the radiometric resolution *Kp* of the ASCAT level 1b product. The full resolution measurements $\sigma_{k,b}{}^0$ are assumed to be normal distributed random variables with mean $\overline{\sigma}_b{}^0$ and variance $Var\left(\sigma_{k,b}{}^0\right)$. The *Kp* value is computed for all three beams $b \in ($ *for, mid, aft*$)$ as well as the mean of the full resolution measurements $\overline{\sigma}_b{}^0 = mean\left(\sigma_{k,b}{}^0\right)$ in the linear domain. Where k labels the individual full resolution measurement in the resampling Hamming window. Rewriting Equation 2.8 allows the calculation of the variance of $\sigma_{k,b}{}^0$ by

$$Var\left(\sigma_{k,b}{}^0\right) = \left(Kp_b \cdot \overline{\sigma}_{k,b}{}^0\right)^2 \qquad (2.22)$$

For every satellite pass we get a new backscatter triplet $[i]$ with $i = 1, \ldots, M$ and $M = $ *number of satellite passes*. We assume a normal distribution with mean μ_i and variance σ_i^2 for each backscatter coefficient of the time series.

Using Equations 2.12, 2.14 and 2.22 the mean μ_i and variance σ_i^2 for the ith satellite pass are given by

$$\mu_i = \delta_i, \tag{2.23}$$

$$\begin{aligned}
\sigma_i^2 =& Var\left(\sigma_{for}^0\right)_i + Var\left(\sigma_{aft}^0\right)_i = \\
& Var\left(\sigma_{k,for}{}^0\right)_i + Var\left(\sigma_{k,aft}{}^0\right)_i = \\
& \left(Kp_{i,for}{\cdot}\overline{\sigma}_{i,for}{}^0\right)^2 + \left(Kp_{i,aft}{\cdot}\overline{\sigma}_{i,aft}{}^0\right)^2.
\end{aligned} \tag{2.24}$$

where $Kp_{i,for}$ and $Kp_{i,aft}$ denotes the radiometric resolution and $\sigma_{i,for}{}^0$ and $\sigma_{i,aft}{}^0$ the backscatter coefficient of the ith satellite path, measured with the *for*- and *aft*-antenna, respectively. The maximum likelihood of estimates of μ_i and σ_i^2 can be expressed by a weighted sample mean and a weighted sample variance as shown in section 2.5.

For every $i = 1, \ldots, M$ we get a normal distribution weighted with $p_i = 1/M$ and $\mu_i = \delta_i = 0$

$$\alpha = \sum_{i=1}^{M} p_i{\cdot}0 = 0 \tag{2.25}$$

$$\beta = \sum_{i=1}^{M} \frac{1}{M} \cdot \sigma_i^2 \tag{2.26}$$

Under the assumption that every measurement of $\overline{\sigma}_{i,b}{}^0$ is a normal distribution with individual mean and variance it is possible to calculate the overall

variance and mean applying to the equations of the Gaussian Mixture Model.

Therefore, equations 2.24 and 2.22, Equation 2.26 are rewritten

$$\beta = \sum_{i=1}^{M} \frac{1}{M} \sigma_i^2 = \sum_{i=1}^{M} \frac{1}{M} \left\{ Var \left(\sigma^0_{for} \right)_i + Var \left(\sigma^0_{aft} \right)_i \right\} \qquad (2.27)$$

where the maximum likelihood estimate of β is the variance of the overall distribution (see section 2.5). The overall distribution is the time series of the backscatter coefficients σ^0 and thus rewriting Equation 2.27

$$ESD_{Kp} \left(\sigma^0 \right) = \sqrt{ \sum_{i=1}^{M} \frac{1}{M} \left\{ Var \left(\sigma^0_{for} \right)_i + Var \left(\sigma^0_{aft} \right)_i \right\} }, \qquad (2.28)$$

where $ESD_{kp} \left(\sigma^0 \right)$ denotes an estimate based on the radiometric resolution Kp. The radiometric resolution Kp is calculated in the linear domain, subsequently the $ESD_{kp} \left(\sigma^0 \right)$ given here is defined in the linear domain. For a comparison of the common ESD and the ESD_{kp} we use an expression, approximating the variance of logarithmic values f of linear data as given by Harris [36]:

$$f = a \log_{10}(A), \quad \sigma_f^2 \approx \left(a \frac{\sigma_A}{A \ln(10)} \right)^2 \qquad (2.29)$$

where σ_f denotes the variance of the logarithmic data and σ_A the variance of the data in linear units. According to equation 2.29 we can calculate the variances in the logarithmic range:

$$Var \left(\sigma^0_{b,i} \right) [dB] \approx \left(10 \frac{\sqrt{Var \left(\sigma^0_{b,i} \right)}}{\sigma^0_{b,i} \ln(10)} \right)^2 \qquad (2.30)$$

2.7   Description of Study Areas

In the present work four areas in various climates showing different biomes are analyzed using the statistical framework evaluated in the section 2.6. In this part, the climates of different test-sites are described. Figure 2.13 shows the locations of four sites in four countries: Niger (A), Western Australia (B), Wyoming USA (C) and Yakutia lowlands, Russia (d). Table 2.1 portrays the main characteristics of each site in terms of location, and climate (mean annual rainfall and temperature). For all the sites the climate is dry or very dry with total average yearly precipitation ranging from 130 mm in Niger to 283 mm in Australian site [37] (see Figure 2.16). More specifically, the biome at the site in Niger can be classified as arid desert. West Australian site is scrubland with low-, but evenly spread rainfall throughout the year and is classified as semi-arid desert. The site in Wyoming, USA with below zero temperatures during the winter months is therefore cold semiarid desert. The Yakutia area can be defined as taiga [38]. Overall, for the soil moisture time series are characterized by various seasonalities. The site in Niger has very little rainfall, from which 96 % of the total yearly precipitation occurs during the summer with extremely high temperatures and close to no rain in winter. At the sites in Wyoming USA and in Western Australian the little rainfall is somewhat evenly spread throughout the year, May and June being the rainiest months. During this period approximately one third of precipitation falls in the site in Wyoming and quarter in the Western Australian site. In

Figure 2.13: Locations of four sites in four countries: Niger (a), Western Australia (b), Wyoming USA (c) and Yakutia lowlands, Russia (d) [39].

Yakutia lowland in Russia, nearly two third of rainfall occurs between June and October. There, more than half year between October and April the average temperature stays below freezing point [37].

Niger

The study area with GPI 920587 is located in Niger, 170km east of Aigadez, where the Sahara desert reaches the Sahel zone. The climate in Niger is characteristically dry arid desert climate. This climate zone has very hot summers and mild winter and scarce precipitation throughout the year. The rainfall is little during the summer and next to none-existent from October to May [46]. The annual average rainfall in the study area is 16 mm/month and the mean temperature of 28 °C, with high annual mean 35 °C and low 21°C. Most of its rain falls between June and September, and rainfall totals of more than 95 % during this season from average total of 130 mm yearly precipitation (see Figure 2.16 (a)) [37]. Vegetation at the
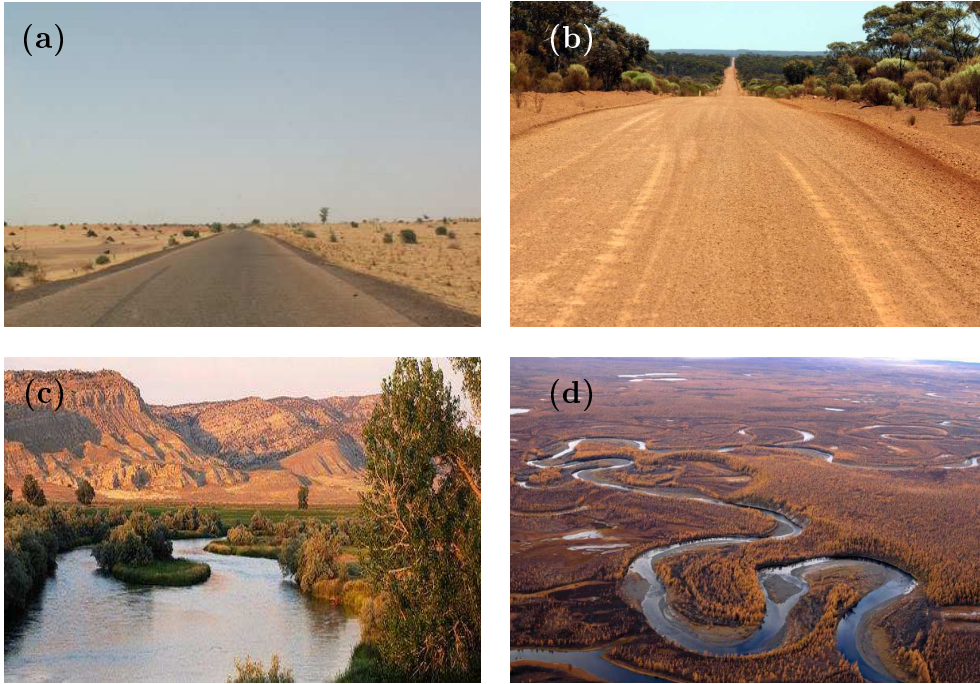
Figure 2.14: Images of study areas, giving an impression of the vegetation. (a) Sahara, Niger [40]; (b) Western Australia [41]; (c) Bighorn river, Wyoming [42] and (d) Yakutia [43];.

site is sparse; mainly scrub bushes and cactus plants [31]. The topography is dominated by longitudinal dunes [47], which are predominately in Western Shara [48] p. 502, on a more or less flat plateau, orientation from north east to south west (see Figure 2.15 (a)). This is caused by the northeast trade wind at this site, with a wind direction of approximately 45° with respect to the satellite flight direction [49, 50]. The azimuthal error of sand is rather caused by small ripples on the dunes than by themselves. Such ripples are aligned transversal to the wind direction [51], thus they are aligned rectangular to the dunes.

Western Australia

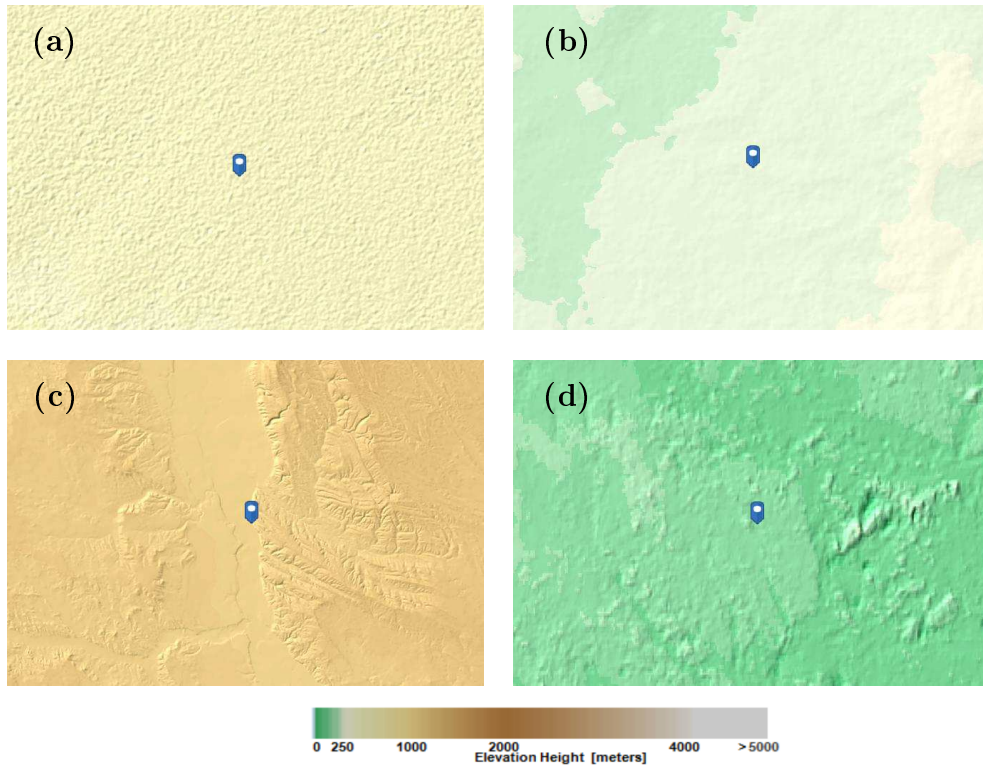This study site is located at Western Australia close to lake Cowan. It is

Figure 2.15: Topography (a): Sahara, Niger; (b): Western Australia; (c): Bighorn river, Wyoming; (d): Yakutia; [39]

relatively dry semi-arid desert climate. This climate zone has hot summers and mild winter and low precipitation [46]. The rain is relatively evenly spread throughout the year and the mean yearly precipitation is 283 mm (see Figure 2.16 (b)) [37]. The general soil type is flat and largely lacking of vegetation, whereas the margins of the lake and fringing dunes and plains have a number of distinct plant communities [52] At this site, the vegetation is mainly shrubs [31]. This site is topographically marginally structured and more or less flat as shown in Figure 2.15 (b).

Wyoming USA

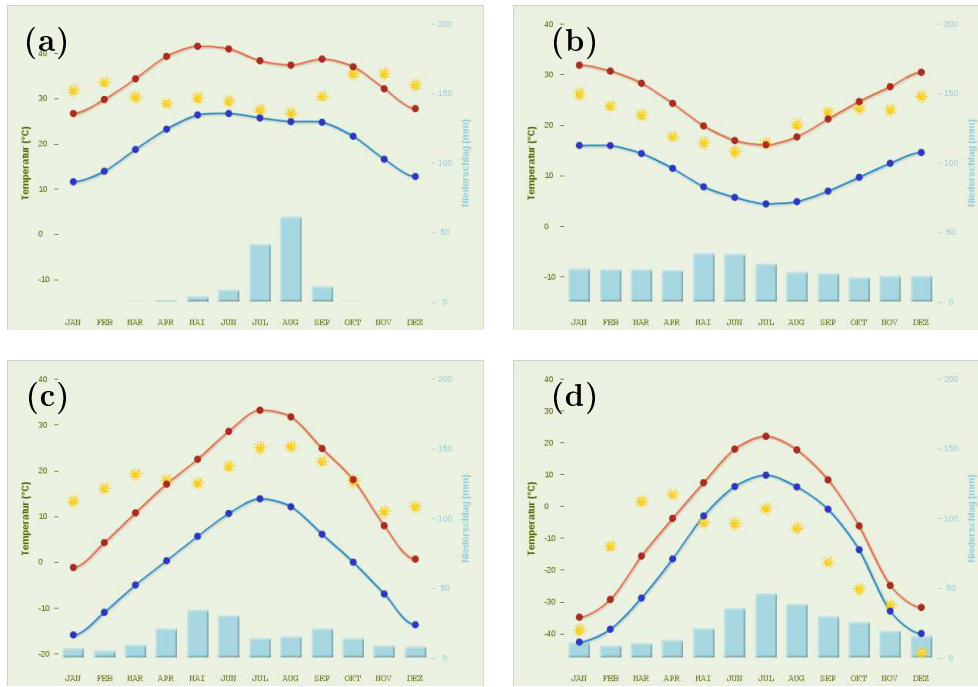GPI: 2277126, Wyoming USA is located close to the city of Basin, area

Figure 2.16: Climate data (a): Sahara, Niger; (b): Western Australia; (c): Bighorn river, Wyoming; (d): Yakutia; [37, 44].

of Bighorn river. The annual average rainfall in this area is 16 mm/month and the mean temperature 7 °C, where high annual mean 16 °C and low -1°C. The mean temperature is above zero most of the year a part from winter moths from December to February. The yearly rainfall totals 190 mm per year from which 85 % occur during the period from April to June (see Figure 2.16 (c)) [37]. The climate in this area is cool semiarid desert. This climate zone is similar to arid climate, but more moderate, experiencing less of the extreme high or low temperatures. It has relatively hot summers and cool winters and low precipitation throughout the year [46]. Here, the vegetation is mainly grasses and shrubs [31]. The topography at this site is dominated by the flat Bighorn river valley surrounded by rugged hills as can be seen in Figure 2.15 (c).

Table 2.1: The main characteristics of the sites used for this study.

Location	Niger	Western Australia	Wyoming USA	Yakutia, Russia
GPI	920587	1712495	2277126	2970343
Lat(°) [38]	16.50	-31.74	44.25	65.57
Lon(°) [38]	9.72	122.15	-108.01	119.15
Elev (m) [45]	398.6	317.1	1269.4	194.9
Rainfall (mm/y) [37]	130	283	190	270
Mean rainfall (mm/month) [37]	11	24	16	23
Mean temperature (min/max) (°C) [37]	20/35	10/24	-1/16	-16/-6
land coverage type [31]	Barren or Sparsley Vegetated	Scrubland	Mixed Scrubland/Grassland	Deciduous Needleleaf Forrest

Yakutia lowlands, Russia

This site is positioned in North-East Russia with nearest city of Zhigansk. The annual average rainfall is 23 mm/month and the mean temperature of -6 °C. Here the high annual mean -6 °C and low -16°C. Annual precipitation mean is 270 mm [37]. This climate zone is subarctic zone, with short, cool summers and long, extremely cold winters. Most of the precipitation falls during the summer. Freezes are common in this area, even in midsummer. Snow arrives early in the fall and lasts on the ground from November to March [53]. Vegetation is typical taiga with Siberian larch with a layer of low shrub beneath, named as deciduous needleleaf forest [31]. The forest floor is covered by mosses, liverworts, and lichens. The growing season defined as the period with at least five days with a daily averaged temperature above 5°C [53] is form May to September (see Figure 2.16 (d)). The topography at this site is more or less flat with little surface roughness. (see Figure 2.15 (d)).

Chapter 3

Experiments and Analyses

3.1 Backscatter and difference of backscatter

In Figure 3.1 on the left panels (a-d) the backscatter σ^0 of the *for*- and *aft*-beam is depicted as time series ranging from 01.01.2007 to 07.19.2015, measured for all study areas. The panels aligned horizontally are showing the backscatter data of one distinctive study area, indicated by the GPI in the left panels (a-d). From top to bottom the panels show the backscatter data of the study site in following order:

(a) Niger, Sahara desert

(b) Western Australia

(c) Bighorn river, Wyoming USA

(d) Yakutia lowlands, Siberia Russia

The measurements correspond to study areas in Australia, USA and Russia, (see Figure 3.1 (c-d)) show a seasonal variation of the backscatter data,

whereas for the study area in Niger no seasonal variation of the backscatter is observed (Figure 3.1 (a)). A statistical summary of the backscatter values σ^0 is shown in the right panels (e-h) of Figure 3.1 as histogram and in Figure 3.2as box plot, respectively. The whisker in the box plot is defined as the maximum of 1.5 times the interquartile range. The median of the backscatter is significantly lower for the study area in Niger compared to the values of the other study areas, as this site in Niger is located in the hyper arid Sahara desert. Furthermore, the backscatter σ^0 from this study area show a significant higher variation compared to the other study area. The most intense backscatter signal is observed from the study area in Yakutia, covered with Taiga and boreal forest. The backscatter, corresponding to this site, reveals a lower variation level. In general, the variation level is correlated with the median value of the backscatter.

Figure 3.3 shows the backscatter difference δ between the fore and after antenna backscatter σ^0, plotted in the left panels (a-d). corresponding to study areas in the same order as in Figure 3.1. The backscatter difference is shown separately for signals measured during an ascending and descending path, depicted as blue and red symbols, respectively. The backscatter σ^0 from the study area in Niger reveals a pronounced seasonal variability, whereas the other sites have no (b, c) or weak (d) seasonal variance. A statistical summary of the backscatter difference values δ is given as histogram in the left panels (e-h) of Figure 3.3 and as box plot in Figure 3.4. The median of the δ values for the ascending and descending paths differs for all study areas. This effects is most pronounced for the study area in Yakutia, and is much lower the other study ares. Furthermore, the distributions of the δ values corresponding to this site, revels two distinct maxima (see Figure 3.3 (e)). The distributions,
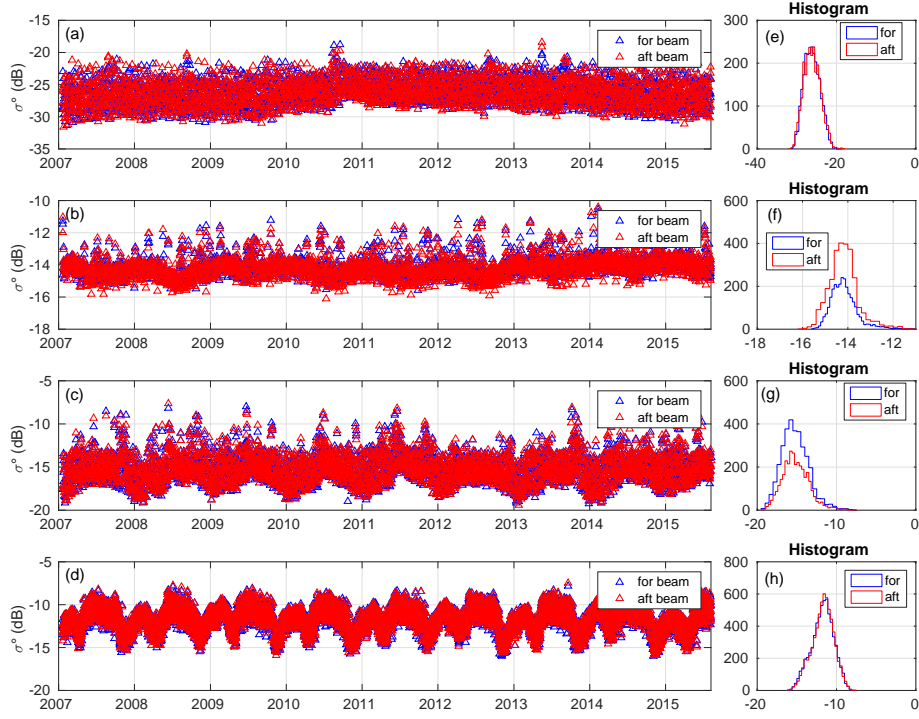
Figure 3.1: Backscatter measured between 2007 and 2015 for all study areas.

corresponding to the other study areas, exhibit one maximum. The median of the ascending path values is lager than the median of the descending paths values the two sites in Niger and Australia, while for the other two sites a converse relation is observed. In the distribution of the δ values two maxima are observed for the data corresponding to the sites in Niger and Australian study area (see Figure 3.3 (e,f)). For the two sites in USA and Russia the distribution of the δ values reveal one maximum (see Figure 3.3 (g,h)).

The seasonal variability of the backscatter difference corresponding to the Niger site, is shown more clearly, in Figure 3.5 (a), where the backscatter difference is displayed separately for the two swath of ASCAT. The backscatter difference of swath 0 exhibit a seasonal oscillation with a minimum around
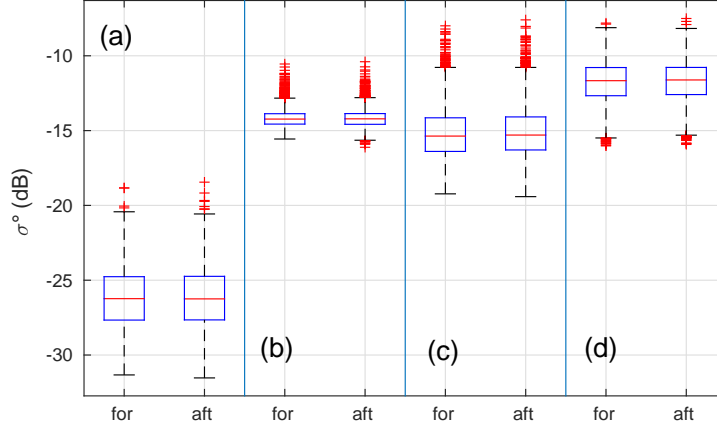
Figure 3.2: Statistic of backscatter.

August and September, which corresponds with the seasonal rain falls between June and September at this site (see Figure 2.15 (a)). Naeimi [54] has shown an increase of the ESD value for areas covered with sand dunes. This increase of the azimuthal noise is caused by a surface and volume scattering of small sand ripples. The observed minimum in the backscatter difference during the seasonal rainfall may be caused by the increase of soil moisture, which prevents the formation of dunes.

In contrast, the seasonal variability of the backscatter difference for the Yakutia site is seen more clearly in Figure 3.3 (d), where the data are displayed for ascending and descending paths by different colored symbols. Furthermore the backscatter data from this site show a pronounced seasonality, with a maximum period during the summer month and a smaller maximum in February 3.1 (d). The summer maximum correlates with the growing season (see Figure 2.16 (d)) of the deciduous needleleaf forest at this site. The dense vegetation during summer month leads to an increase of backscatter and a decrease of the ESD for this study site. From November to march
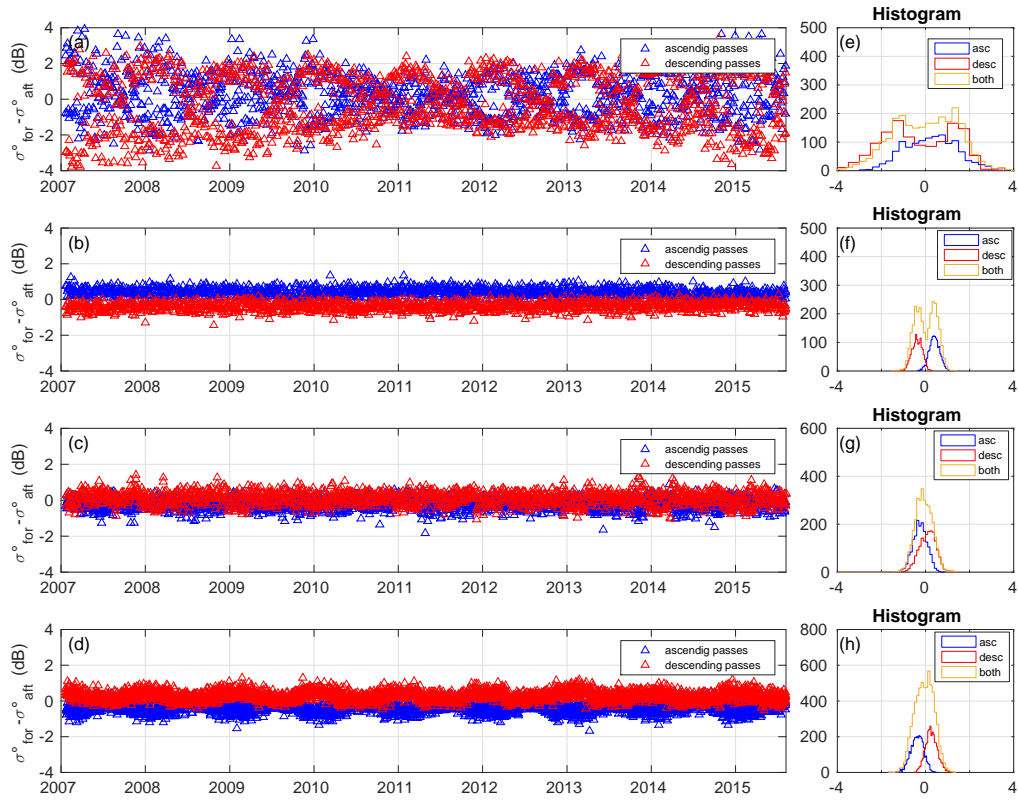
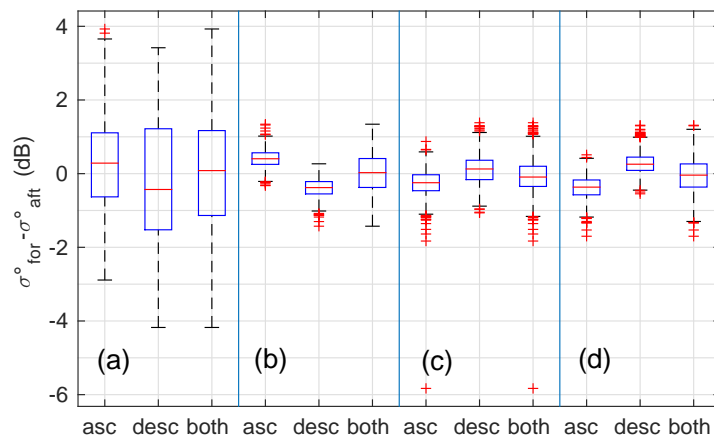**Figure 3.3:** Difference of backscatter data measured during an ascending or descending path.

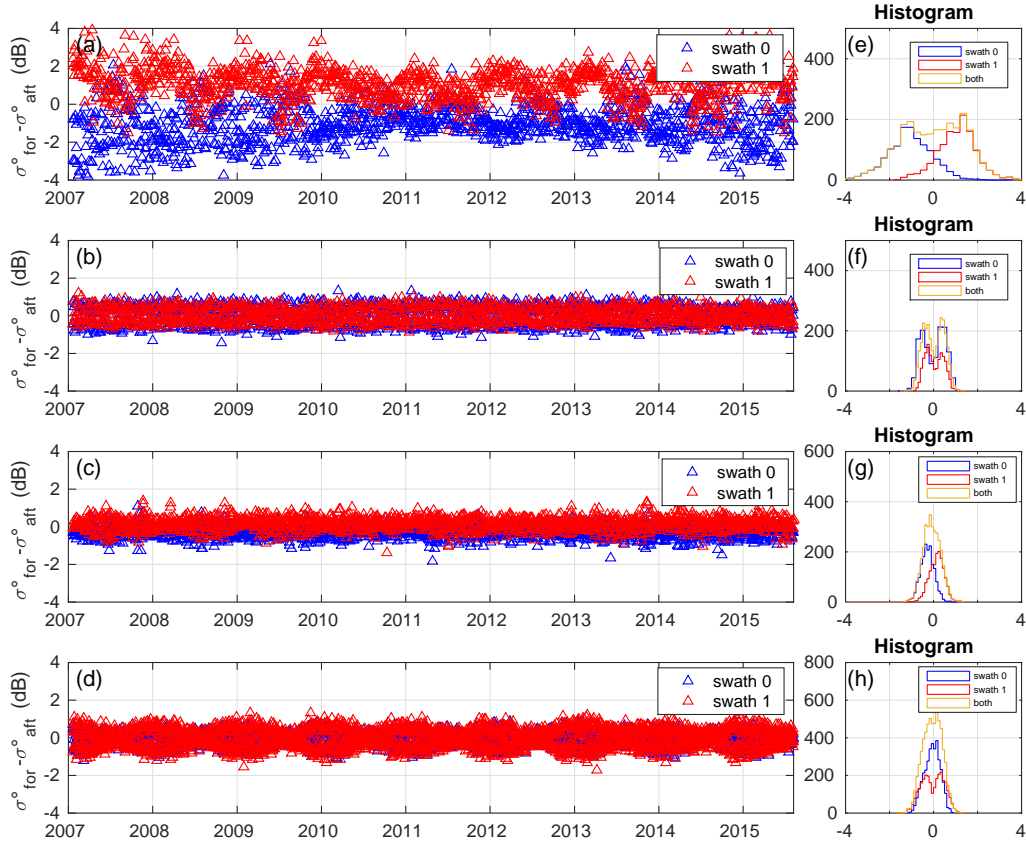**Figure 3.4:** Statistic of delta values.

Figure 3.5: Difference of backscatter data, corresponding to the different swath of ASCAT.

this site is covered with snow, which corresponding to the winter maximum of the backscatter. Frozen soil leads to a decrease of the backscatter [55], and dry snow is more or less transparent at C-Band. This is in contrast to the observation of an winter maximum of the backscatter. For wet snow the dominating scattering mechanism is surface scattering and the backscatter intensity depends on snow surface roughness [55]. Maybe this causes the winter maximum of backscatter. The seasonal variation of the backscatter difference is caused by the dense vegetation during the the growth season (summer minimum) and the azimuthal effect of the surface roughness (win-

Table 3.1: ESD for all study area sites

study area		(a)	(b)	(c)	(d)
land cover	Ref. [31]	Barren or	Scrubland	Mixed Scrubland/	Mixed
		Sparsley Vegetated		Grassland	Tundra
ESD (dB)	Eq. 2.16	1.015	0.327	0.287	0.303
ESD_{Kp} (dB)	Eq. 2.28	0.257	0.204	0.17	0.149
ESD/ESD_{Kp}		4.0	1.6	1.7	2.0

ter maximum) (see Figure 3.3 (d)).

In Figure 3.3 (b-d) the backscatter differences have equal absolute values but opposite signs corresponding to the ascending or descending path. This is caused by the reverse alignment of the ASCAT antennas with respect to the observed point on Earth's surface, during an ascending path compared to a descending path. The backscatter difference of the Niger site in Figure 3.3 (a) corresponding to the ascending or descending path, split in patterns of the data with opposite variability, one corresponding to swath 0 and the other to swath 1 of ASCAT, resulting in the two maximum of the distributions. In Figure 3.5 the data corresponds to both swaths of ASCAT are plotted by different colored symbols reveal a more or less mirror like seasonal variability. This fact causes the opposite sign of the backscatter difference values because of the ascending and descending orbits (see Figure 3.5 (a)).

Using Equation 2.16 the ESD(σ^0) value is calculated for all study areas (see Table 3.1). The calculated $ESD(\sigma^0)$ values of the study areas are within the ESD range of the corresponding land cover type in Figure 2.11. The land cover type was determined by the Global Land Cover Classification (GLCC) database [31]. The images in Figure 2.14 gives an impression of the land cover type of the study areas. The figures where found on the internet [40], [41], [42], [43] taken at locations close to the study areas.

3.2   Radiometric resolution Kp

In Figure 3.6 (a-d) the Kp values of the fore, mid and aft beam, labeled by *for, mid* and *aft*, are plotted as time series measured between 01.01.2007 and 07.19.2015, corresponding to study area in Nigeria (a), Australia (b), USA (c) and Russia (d). In panels (e-h) the histograms of the Kp values are shown. The panels (i-l) show the distribution of the square root of the variance, calculated by Equation 2.22 and converted into the logarithmic range using Equation 2.29 for the *for-*, *mid* and *aft*-beam. Using Equations 2.28 and 2.29 the ESD_{Kp} value is calculated in the logarithmic range and is marked as vertical line in Figure 3.6 (i-l), respectively. In addition, the ESD given by Equation 2.16 is marked in the panels (i-l). Note the different scaling of the panel (i). It is obvious, the Kp values of the *for-* and *aft*-beam displays a similar distribution for all study areas, whereas the distribution of the *mid*-beam is different.

In contrast to the backscatter difference the radiometric resolution Kp does not show any seasonal variability. A statistical summary of the Kp values is given in Figures 3.7 and 3.6 (e-f). The median and the interquartile range of the Kp values decreases for the particular study areas, going from left to right corresponding to the Kp values in Figure 3.6 (a-d), respectively.

3.3   Impact of azimuthal noise on ESD and ESD$_{Kp}$

In Figure 3.8 (a-d) the distribution of the $\delta = \sigma_{for}^0 - \sigma_{aft}^0$ values is shown as histogram where the mean value and the standard deviation are marked by vertical lines. These distributions are compared to the standard deviation which is calculated as the square root of the variance $Var[\sigma^0]$ by using
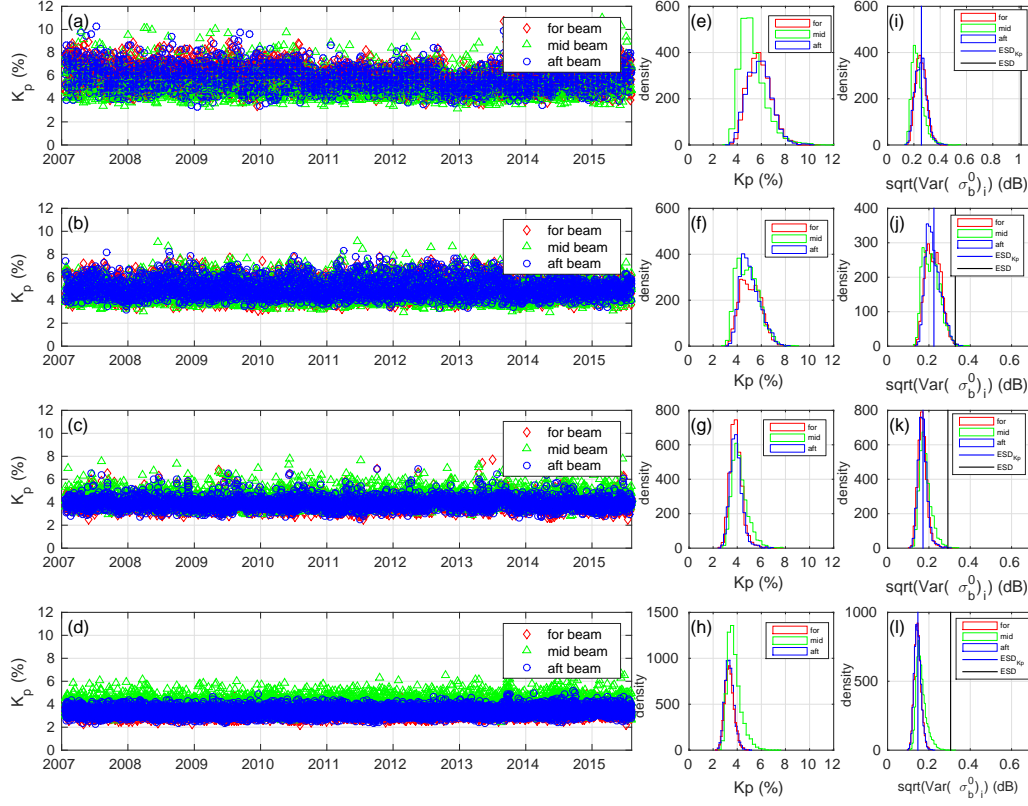
Figure 3.6: Kp data of the three antennas (*for, mid* and *aft*) in a time period ranging from 2007 to 2015.
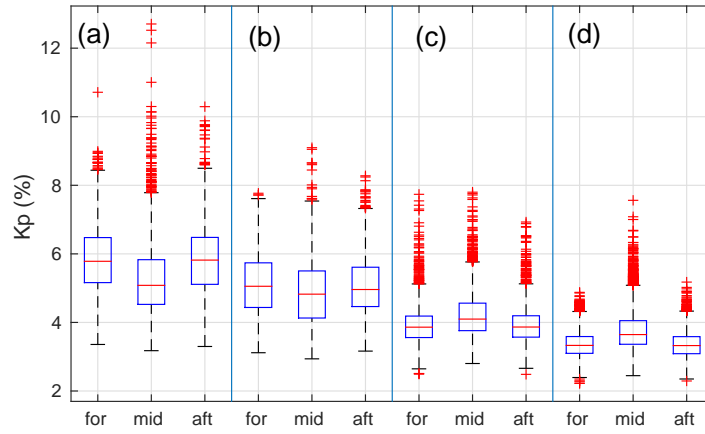

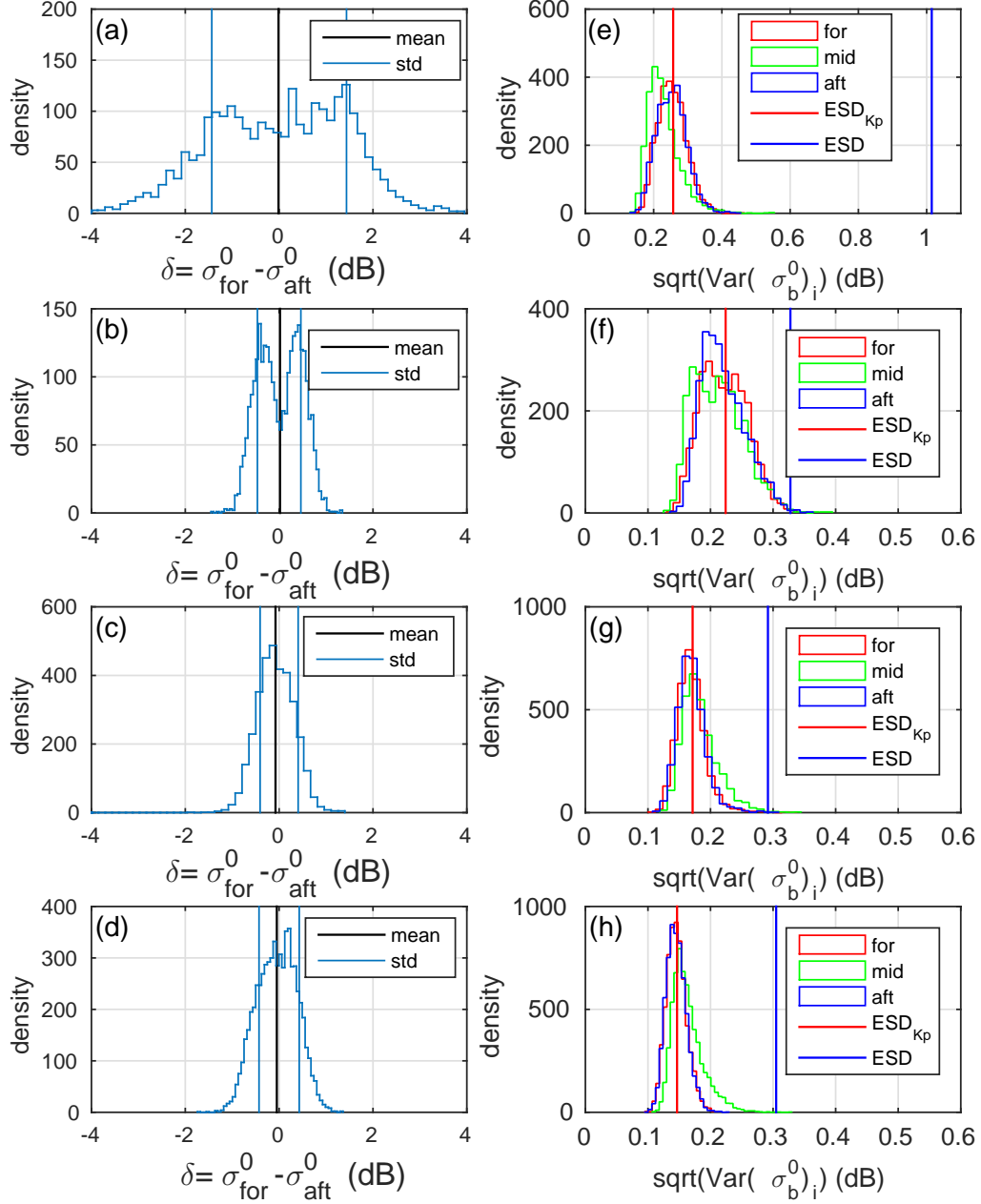**Figure 3.7:** Statistic of Kp data.

Figure 3.8: (a-d): Histogram of $\delta = \sigma_{for}^0 - \sigma_{aft}^0$ values. The mean value and the standard deviation are marked by vertical lines. (e-h): Histogram of the square root of the variance given by Eq. 2.22, the red vertical line marks the $ESD_{Kp}(\sigma^0)$ and the blue vertical line the $ESD(\sigma^0)$.

Table 3.2: Different ESD values calculate for various sites. In the last column the ratio of $ESD(\sigma^0)/ESD_{Kp}(\sigma^0)$ is given, showing an value grater then 3 for the arid sites.

GPI	site	Lon (°)	Lat (°)	ESD	ESD$_{Kp}$	ESD/ESD$_{Kp}$
1104677	Madagascar	46.8	-19.9	0.187	0.162	1.156
1158929	Saudi Arabia	50.9	20.9	3.297	0.416	7.933
1455307	Australia	137.7	-26.5	0.528	0.236	2.239
1503065	South Africa	-21.9	27.6	0.292	0.169	1.727
1511629	China, Hunan	113.3	27.7	0.176	0.190	0.929
1749480	Alabama USA	-87.3	32.5	0.154	0.156	0.985
2076073	China, Tarim basin	83.9	39.6	2.882	0.259	11.118
2395539	Salzburg, Austria	12.6	47.4	0.257	0.178	1.444
2691807	Moscow, Russia	55.7	37.6	0.237	0.302	0.786
2874617	Norway	8.3	61.9	0.293	0.211	1.391
2945077	Western Siberia, Russia	61.3	64.6	0.169	0.160	1.059
3158140	Greenland	-48.1	75.4	0.614	0.157	3.910
376668	Basil, rain forest	-68.1	-6.7	0.129	0.140	0.922
6831	Sumatra,rain forest	101.7	-0.1	0.140	0.146	0.960

Eq. 2.22, shown in Figure 3.8 (f-h). In Figure 3.8 the panels aligned horizontally, correspond to one distinctive study area identified by the label (a-d) in the left panels. In panels (e-h) the red vertical line marks the $ESD_{Kp}(\sigma^0)$ and the blue vertical line the $ESD(\sigma^0)$. Note the different scaling of the x-coordinate of panel (e) compared to panels (f-h). Figure 3.8 illustrates the difference between the common ESD and the ESD_{Kp}, panel (a) show the broad distribution of the backscatter difference δ of site (a) with the two distinct maxima close to the standard deviation. Also in panel (b) the two maxima, resulting from the of residual azimuthal effects depicted in the different overpasses, of the *for*- and *aft*-beam are visible. The high ESD value in (e) reflects the broad distribution of δ, whereas the ESD_{Kp} has a much smaller value. This difference between ESD and ESD_{Kp} is observed also for the other sites (b-d).

The values of different ESD quantities $ESD(\sigma^0)$ and $ESD(\sigma^0)_{Kp})$ used in this work are summarized in Table 3.1. It is obvious that the $ESD(\sigma^0)$ and $ESD_{Kp}(\sigma^0)$ quantities differ in their values. Thus we compare the ratios between the $ESD(\sigma^0)$ and $ESD_{Kp}(\sigma^0)$ values. The ratios, corresponding to the sites in Australia, USA and Russia, have similar values (1.6-2), but for the site in Niger this ratio is at least twice as large (4.0).

From the previous analysis of the ESD and ESD_{Kp} it is obvious that both quantities have a different dependence on azimuthal effects. The common ESD is strongly affected by azimuthal noise, whereas for the ESD_{Kp} no influence of the azimuthal dependence is observed.

This is confirmed by the $ESD(\sigma^0)$ values in Table 3.2 of various locations. For these areas no detailed description is given in section 2.7, however it is obvious that the arid sites in Saudi Arabia, the site located in the Taklamakan and in Greenland have values greater than 3, as sand-dunes and snow show a pronounced azimuthal effects. In comparison the areas covered with rain forest in Basil and Sumatra and the wetland areas in Alabama and Hunan in China reveal ESD ratios smaller than 1. The dense vegetation coverage at this sites leads to a strong volume scattering of the microwaves which result in small or negligible azimuthal effects.

3.4   Time dependence of ESD and ESD$_{\text{Kp}}$

In Figures 3.9 and 3.10 a short period ESD values is plotted, calculated by averaging 20 data points, which corresponds approximately to 12 days. This period is selected as it drastically smoothing the original time series, whereas the seasonal behavior is not affected. The averaged ESD varies distinctively with a periodicity of a year for the study areas located in Niger
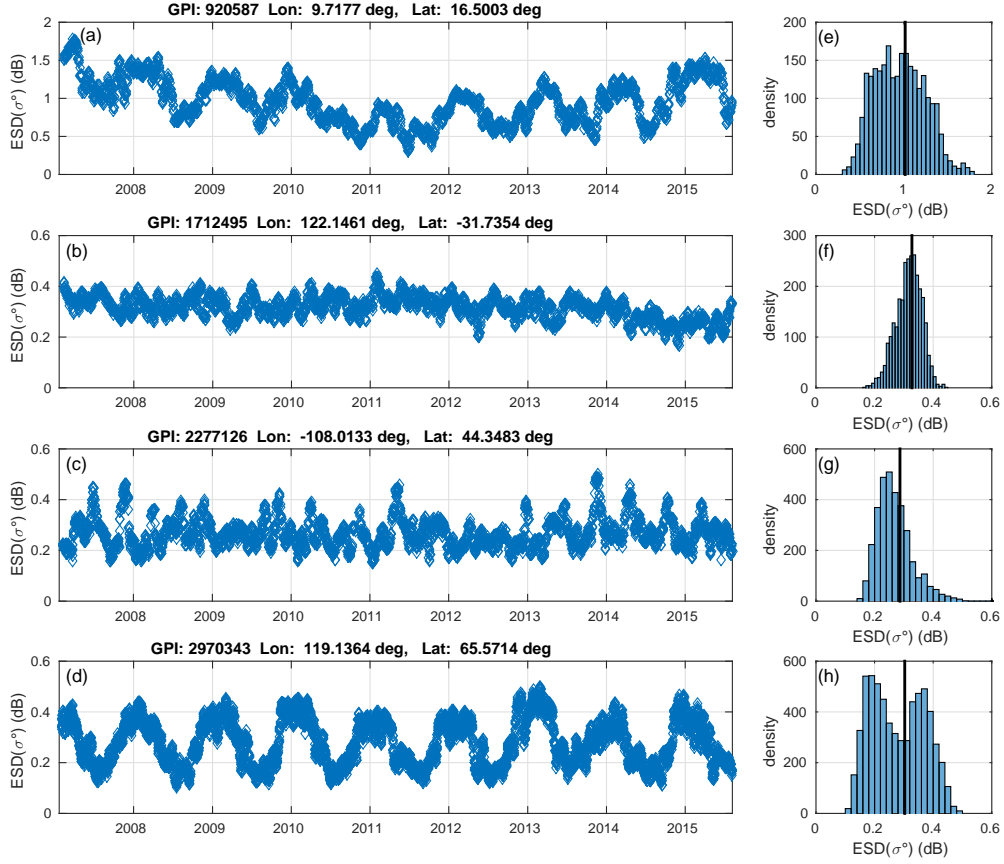
Figure 3.9: Averaged *ESD* value calculated for 20 data points.

and Yakutia in Figure 3.9 (a) and (d) and the averaged *ESD* corresponding to the study area in Wyoming in Figure 3.9 (c) show peak-like features, with no temporal periodicity. The azimuthal effects described in section 3.1 causes the pronounced seasonality of the short period *ESD* in Figures 3.9 (a,d). In addition, the area in Yakutia reveals a long time variation during a period of several years. The averaged *ESD* values are summarized in the histograms on the right panels in Figure 3.9 (e-h) together with the *ESD* value marked as vertical black line. For the averaged ESD_{Kp} value only weak seasonal variability is observed for site (a), for the other sites (b-d) no
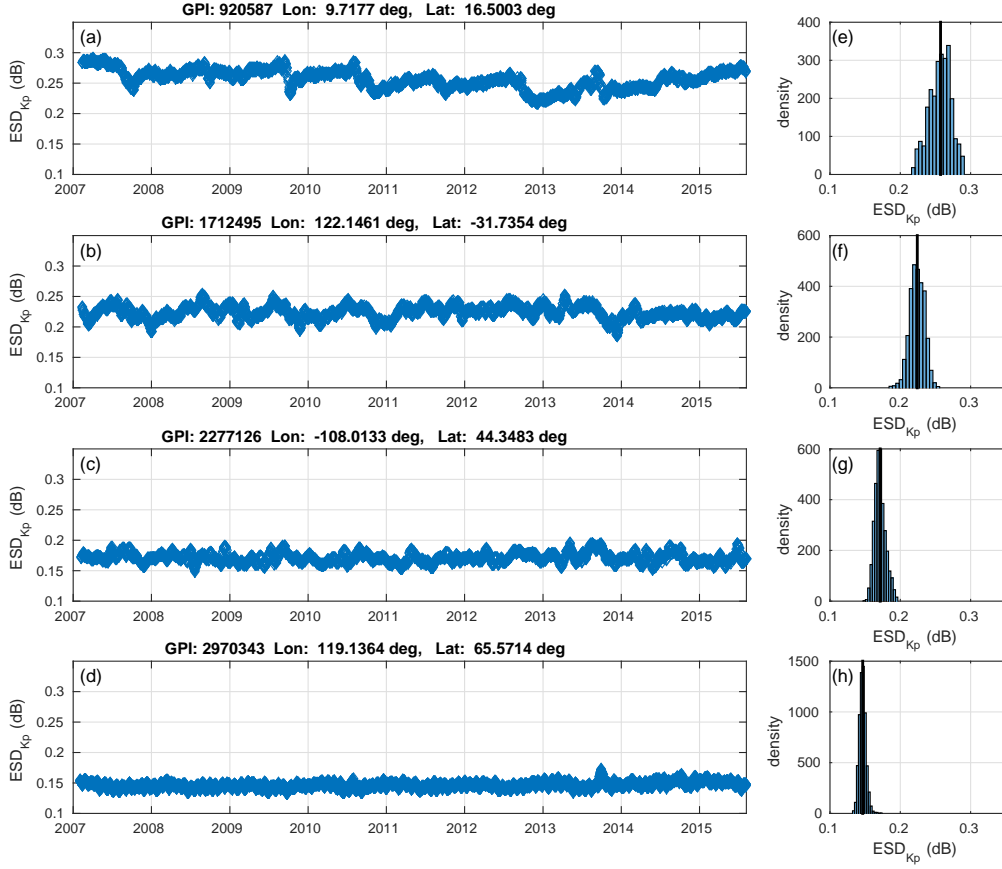
Figure 3.10: Averaged ESD_{Kp} value calculated for 20 data points.

temporal variation is observed. This behavior additionally highlights the low impact of the azimuthal effects on the ESD_{Kp} quantity.

Figure 3.11 show the cumulative calculated ESD (a-d) and ESD_{Kp} (e-h) values, for all study areas in the usual order, respectively. The values are calculated with an increasing length of the time series used Equation 2.16 and 2.28, ranging from three measurements to the entirely available backscatter data. The horizontal black line marks the ESD values calculated with all data point. The data shows that the ESD_{Kp} value reaches much faster the long term value compared with the ESD values. For the ESD_{Kp}, a reliable
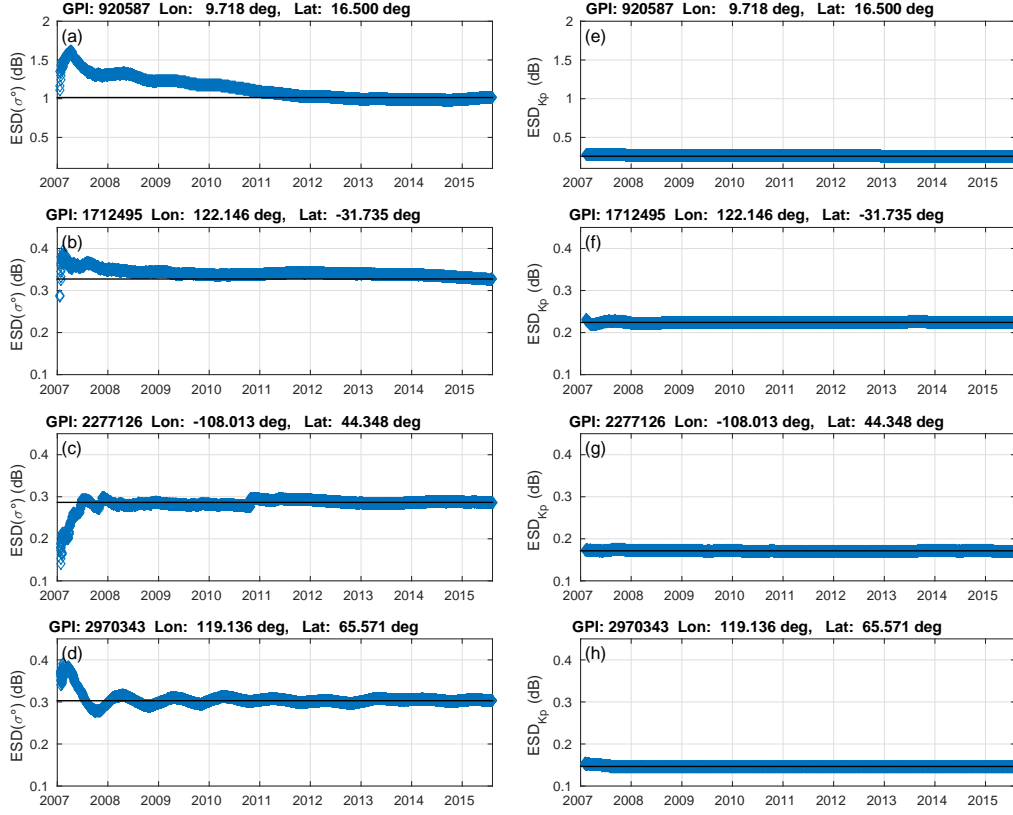
Figure 3.11: Cumulative calculated ESD (a-d) and ESD_{Kp} (e-h) values. The horizontal black line marks the ESD values calculated with all data points.

value is calculated with data of at least one year, while for the ESD value data of several years is required.

Comparing the two ESD_{Kp} quantities reveals a difference in several aspects. Firstly the ESD parameters alters on different values and it is dependent on the azimuthal effects of the corresponding study area. Secondly the two different ESD parameters have a diverging temporal dependence. The ESD_{Kp} reaches an robust value within month, as for the ESD, data from several years is necessary for a robust estimation. Thus, this ESD parameter

show a pronounced seasonal variation for a averaging over some twelve days whereas the averaged ESD_{Kp} varies much less with time.

Chapter 4

Conclusion & Outlook

In the analysis of the relationship and differences of the current estimation of the standard deviation of backscatter ESD and the standard deviation information Kp a new expression ESD_{Kp} was given, defining a relationship between ESD and Kp. Comparing the two ESD quantities reveals a low impact of the azimuthal effects on the ESD_{Kp}, whereas the ESD strongly depends on the azimuthal effects. Subsequently the ESD values differ from the ESD_{kp} values. In this work a ratio of approximately 1.8 was found between the ESD and ESD_{Kp} values for areas with moderate azimuthal effects. For a hyper arid study area revealing an intense azimuthal effect this ratio was found to be twice as high. The ESD_{Kp} value can bee considered as dynamic estimated standard deviation of the backscatter, as it is calculated for all individual measurements of a time series. For the current ESD quantity long time measurements of several years are needed for a robust estimation.

In the present work ESD values of four sites were studied. For a more reliable comparison of the different ESD types a larger group of study areas needs to be analyzed. Thus no analytical expression could be found describing the relationship of the two ESD quantities. Nevertheless, a rough trend

can be seen as a result of this research. The research in this work reveals a first insight on the new ESD_{Kp}, especially the disparity among the common ESD and the new ESD_{Kp} has been elaborated. It is up to further research activities to demonstrate the usefulness of the new ESD_{Kp} to enhance the uncertainty estimation of backscatter.

Bibliography

[1] EUMETSAT [Online], October (2015).
http://www.eumetsat.int/website/home/index.html.

[2] Verspeek JA, Stoffelen A, Portabella M, Bonekamp H, Anderson C and Figa J, Validation and calibration of ASCAT using CMOD5.n, *Trans. Geosci. & Rem. Sens*, 48, pp 386-395, (2010).

[3] Bartalis Z, Wagner W, Naeimi V, Hasenauer S, Scipal K, Bonekamp H, Figa J and Anderson C , Initial soil moisture retrievals from the METOP-A Advanced Scatterometer (ASCAT), *Geophys. Res. Letters*, 34., (2007).

[4] Lavergne T, Eastwood S, Teffah Z, Schyberg H and Breivik LA , Sea ice motion from low-resolution satellite sensors: An alternative method and its validation in the Arctic, *J. Geophys.* Res.115., (2010).

[5] S. Hahn. Calibration-Related Artefacts in the initial ASCAT Soil Moisture Product. Master's thesis, Vienna University of Technology, Austria, (2011).

[6] EUMETSAT [Online], October (2015):
http://oiswww.eumetsat.org/WEBOPS/eps-pg/ASCAT/
ASCAT-PG-4ProdOverview.htm#TOC421.

[7] Z. Bartalis. *Spaceborne Scatterometers for Change Detection over Land.* PhD thesis, Vienna University of Technology, Austria, (2009).

[8] Attema E. P. W.„ The active microwave instrument on-board the ERS-1 satellite„ Proceedings of the IEEE, vol. 79, no. 6, pp. 791–799, (1991).

[9] Gelsthorpe, R.V., Schied, E., and Wilson, J.J.W. ASCAT-MetOp's advanced scatterometer. *ESA Bulletin 102*, (2000). Available at http://esapub.esrin.esa.it/bulletin/bullet102.htm.

[10] S. Hahn, Calibration-Related, Artefacts in the initial ASCAT Soil Moisture Product, master thesis, Vienna University of Technology, Austria,, p. 25, (2011).

[11] EUMETSAT, ASCAT Product Guide, *Tech. rep.*, European Organization for the Exploitation of Meteorological Satellites, Darmstadt, Germany, (2009).

[12] Pierschel, D., AMI Team Active Microwave Instrument Requirements Specification, ESA/ESTEC, Doc. No. ER-RS-DSF-AM-0001, (1988).

[13] Wolfagang Wagner. *Soil Moisture Retrieval form ERS scatterometer Data.* PhD thesis, Vienna University of Technology, Austria, (1998).

[14] Ulaby, F. T., K. Sarabandi, K. McDonald, M. Whitt and M. C. Dobson, Michigan microwave canopy scattering model, *International Journal of Remote Sensing*, Vol. 11, pp. 1223, (1990).

[15] Karam, M. A., A. K. Fung, R. H. Lang and N. S. Chauhan, A microwave scattering model for layered vegetation, *IEEE Transactions on Geoscience and Remote Sensing*, Vol. 30, pp. 767, (1992).

[16] Saatchi, S. S., D. M. Le Vine and R. H. Lang, Microwave backscattering and emission model for grass canopies, *IEEE Transactions on Geoscience and Remote Sensing*, Vol. 32, pp. 177, (1994).

[17] Naeimi V., Model improvements and error characterization for global ERS and METOP scatterometer soil moisture data, Ph.D thesis, Vienna University of Technology, Austria, p. 29 , (2009).

[18] Vahid Naeimi. *Model improvements and error characterization for global ERS and METOP scatterometer soil moisture data.* PhD thesis, Vienna University of Technology, Austria, (2009).

[19] P.-L. Frison an dE. Mougin (1996), *Use of ERS-1 Wind Scatterometer Data over Land Surfaces*, IEEE Transactions on geoscience and remote sensing, Vol. 34, No. 2, (1996).

[20] Wuttge, S., H. Munz, Effects of Gaps in the Scatterometer Raw Data on σ^0-Triplets, ESA, ESRIN, *Doc. No.* ER-TN-DSF-FL-0001, May 1995, p. 95, (1995).

[21] David G., Long and Gary B. Skouson (1996), *Calibration of Spaceborne Scatterometer Using Tropical Rain Forrest*, IEEE Transactions on geoscience and remote sensing, Vol 34, No 2, (1996),.

[22] Fawwaz T. Ulaby. *Fundamentals of applied electromagnetics.* Prentice-Hall, Inc., Upper Saddle River, NJ, USA, (1997).

[23] Early, D. S., D. G. Long, Azimuthal Modulation of C-Band Scatterometer σ^0 Over Southern Ocean Sea Ice, *IEEE Trans. Geosci. Remote Sensing*, Vol. 35, No. 5, pp. 1201-1209, (1997).

[24] Wolfagang Wagner. *Soil Moisture Retrieval form ERS scatterometer Data.* PhD thesis, Vienna University of Technology, Austria, (1998).

[25] Eric W. Weissenstein. Normal differnece Distribution, From MathWorld–A wolfram Web Resource.

[26] Vahid Naeimi. *Model improvements and error characterization for global ERS and METOP scatterometer soil moisture data.* PhD thesis, Vienna University of Technology, Austria, (2009).

[27] Vahid Naeimi. *Model improvements and error characterization for global ERS and METOP scatterometer soil moisture data.* PhD thesis, Vienna University of Technology, Austria, (2009).

[28] Vahid Naeimi. *Model improvements and error characterization for global ERS and METOP scatterometer soil moisture data.* PhD thesis, Vienna University of Technology, Austria, (2009).

[29] Naeimi V., Model improvements and error characterization for global ERS and METOP scatterometer soil moisture data, Ph.D thesis, Vienna University of Technology, Austria, p. 75, (2009).

[30] Naeimi V., Model improvements and error characterization for global ERS and METOP scatterometer soil moisture data, Ph.D thesis, Vienna University of Technology, Austria, p. 77, (2009).

[31] Global Land Cover Classification (GLCC) database, U.S. Geological Survey, October (2015).
http://edc2.usgs.gov/glcc/glcc.php, ftp://edcftp.cr.usgs.gov.

[32] B. Lehner and P. Doll. Global lakes and wetlands database (glwd). World Wildlife Fund, (2004).

[33] GTOP30, Global Digital Elevation Model Datase, U.S. Geological Survey. https://lta.cr.usgs.gov/GTOPO30.

[34] F.T. Ulaby, R.K. Moore, and A.K. Fung. *Microwave Remote Sensing: Radar remote sensing and surface scattering and emission theory.* Artech House remote sensing library. Addison-Wesley Publishing Company, Advanced Book Program/World Science Division, 1981.

[35] Javad Behboodian. On a Mixture of Normal Distributions. *Biometrika*, 57(1):pp. 215–217, (1970).

[36] D.C. Harris. *Quantitative Chemical Analysis, Sixth Edition.* W. H. Freeman, (2003).

[37] GEO Reisecommunity. Klima - Weltweit. [Online], October (2015). http://www.geo.de/reisen/community/klimadaten.

[38] NASA Earth Observatory. Mission: Biomes. [Online], October (2015). http://earthobservatory.nasa.gov/Experiments/Biome/.

[39] ESRI, ArcGIS Desktop [Map]: Release 10. Redlands, CA: Environmental Systems Research Institute, October (2015).
http://www.arcgis.com/home/webmap/viewer.html?useExisting=1,
http://services.arcgisonline.com/ArcGIS/rest/services/
World_Topo_Map/MapServer/0.

[40] Esther Garvi, October (2015).
http://www.esthergarvi.org/2008/04/27/
the-scenery-between-zinder-and-tanout/.

[41] Béatrice Laora Lux und Marco Eberhard, Sennweidstr. 12, 8608 Bu-
     bikon, Schweiz, October (2015).
     http://www.omniversum.info/index.php.

[42] Montana-Wyoming West Ranch Brokerage. PO Box 578,
     Laurel, MT 59044, 406.628.2341 office, October (2015).
     http://01f0c54.netsolhost.com/montwyowest/.

[43] Irek Szatlach, October (2015).
     http://wyprawawedkarska.pl/russia-fishing-trips/trophy-fishing-in-yacutia/.

[44] Climate Data Center, Deutsche Wetterdienst. [Online], October (2015).
     http://www.dwd.de/DE/leistungen/cdcftp/cdcftp.html?nn=17626,
     ftp://ftp-cdc.dwd.de/pub/CDC/.

[45] Teledienstgesetz, Bundesrepublik Deutschland, [Online]., October
     (2015). http://mygeoposition.com.

[46] NOAA - National Oceanic and Atmospheric Administration, United
     States Department of Commerce. NSTA Interactive: Climate Zones.
     [Online], October (2015). http://oceanservice.noaa.gov.

[47] PG-Net. Das Lernportal zur Einführung in die Physische Geographie,
     [Online], October (2015).
     http://www.geo.fu-berlin.de/v/pg-net/geomorphologie/
     aelisches_system/duenen/index.html.

[48] Herbert Louis and Klaus Fischer. *Allgemeine Geomorphologie : Textteil
     u. gesonderter Bilderteil / von Herbert Louis ; unter Mitarb. von Klaus
     Fischer.* de Gruyter Berlin ; New York, 4., erneuerte u. erw. Aufl.
     edition, (1979).

[49] L. Guertin. EARTH 105: Environments of Africa, Lesson 7: Climates
of Africa - Forming of the Sahara Desert, [Online]. Department of
Geosciences, Penn State, October (2015).
https://courseware.e-education.psu.edu/courses/earth105new/
content/lesson07/03.html.

[50] FOOD AND AGRICULTURE ORGANIZATION OF THE UNITED
NATIONS Rome. *Training Manual for TSETSE CONTROL PERSON-
NEL*, j.n. pollock edition, (1982).
http://www.fao.org/docrep/009/p5178e/P5178E11.htm,
ftp://ftp.fao.org/docrep/fao/009/p5178e/p5178e00.pdf.

[51] A. Quadt M. Bartelmann.   Welt der Physik [Online], Deutsche
Physikalische Gesellschaft e.V.
http://www.weltderphysik.de/thema/hinter-den-dingen/strand/wellenmuster/.

[52] Eddie J.B van Etten, Brett Neasham, and Sarah Dalgleish. Soil seed
banks of fringing salt lake vegetation in arid Western Australia â den-
sity, composition and implications for postmine restoration using topsoil.
Ecological Management Restoration, 15(3):239–242, (2014).

[53] GERICS, Climate Service Center. [Online], October (2015).
http://www.climate-service-center.de/033626/index_0033626.html.de.

[54] Vahid Naeimi. *Model improvements and error characterization for global
ERS and METOP scatterometer soil moisture data*. PhD thesis, Vienna
University of Technology, Austria, (2009).

[55] Vahid Naeimi. *Model improvements and error characterization for global
ERS and METOP scatterometer soil moisture data*. PhD thesis, Vienna
University of Technology, Austria, (2009).